Accepted to Phys. Fluids 10.1063/5.0147216

Investigation of the formation and evolution of over-tip shock waves in the pressure-driven tip leakage flow by time-resolved schlieren visualization

Xiaolong Tang (唐小龙),[1, 2, a)] Xiaodong Li (李晓东),[3] Eldad J. Avital,[4] Zainab J. Saleh,[5] and Fariborz Motallebi[4]

[1)]*Shanghai Institute of Applied Mathematics and Mechanics (SIAMM), Shanghai Key Laboratory of Mechanics in Energy Engineering, School of Mechanics and Engineering Science, Shanghai University, Shanghai 200444, China*

[2)]*Key Laboratory of Aerodynamic Noise Control, China Aerodynamics Research and Development Center, Mianyang Sichuan 621000, China*

[3)]*School of Energy and Power Engineering, Beihang University, Beijing 100191, China*

[4)]*School of Engineering and Materials Science, Queen Mary University of London, London E1 4NS, UK*

[5)]*School of Engineering and the Environment, Kingston University London, London KT1 2EE, UK*

([a)]Authors to whom correspondence should be addressed: tangxl@shu.edu.cn)

(Dated: 30 March 2023)

Accepted to Phys. Fluids 10.1063/5.0147216

Time-resolved schlieren visualization and transonic wind tunnel are used to investigate tip leakage flows (TLFs) over several generic blade tip models. Focus is on the generation and evolution of the over-tip shock waves in the clearance region. A multi-cutoff superposition technique is developed to improve the schlieren system for better visualization. Unsteady flow structures such as over-tip shock oscillation, shear-layer flapping, and vortex shedding are revealed by Fourier analysis and dynamic mode decomposition. To predict the generation and decaying of over-tip shocks, a simplified model is proposed by analogizing the shock system to be an N-shaped sawtooth wave. The results show that: (1) The proposed model is able to capture the main features of the generation and decaying of over-tip shock waves. The processes of shock generation, decaying and fading-out are dominated by the mean background flow, the shock state and the flow fluctuations, respectively. Adding extra coming flow fluctuations can be an efficient way to control the evolution of over-tip shock system. (2) The shock-oscillating frequency is kept the same with the shear-layer flapping, and shock waves with a given oscillating frequency range is constrained to a specific position range. This is termed the "lock-in effect", which is also observed in TLFs over contoured blade tips. The non-uniformity generation and the nonlinear propagation of shock waves are responsible for this effect. Constrained by this effect, the evolution of over-tip shock waves is separated into four discrete phases. Thus, this effect can be applied for the control of TLFs.

[a)] Authors to whom correspondence should be addressed: tangxl@shu.edu.cn

Accepted to Phys. Fluids 10.1063/5.0147216

NOMENCLATURE

a	passing height of schlieren image	b_i	DMD mode amplitude
c	tip clearance	c_0	acoustic wave speed
d	spanwise extent of the model	DMD	dynamic mode decomposition
f	frequency	f_m	focal length of schlieren mirror
f_s	sample rate	g	grayscale of images
h	height of slit light source	h_b	height of separation bubble
H	height of wind tunnel	I	intensity of turbulence
K	constant of schlieren system	K_{sv}, K_{sh}	vertical, horizontal schlieren constants
l_{turb}	turbulence length scale	L	length of schlieren extent
$\overline{M}_e$	Mach number at the exit	$\overline{M}_{max}$	maximum Mach number
$n_c \times n_w$	grid size in the clearance	n_p	number of images
P_{out}	static pressure at $x = 350$ mm	P^*	atmospheric pressure
ΔP	$= P^* - P_{out}$, pressure difference	r_p	$= \Delta P / P^*$, ratio of pressure difference
$\bar{P}^*_{ref}$	total pressure at $x = -100$ mm	$\bar{P}^*(x)$	averaged total pressure at x
St_c	Strouhal number by clearance	T^*	total temperature
T1-T3	four time labels	v_x, v_y	velocities
w	width of the model	x, y	coordinates
$\gamma(x)$	normalized grayscale at x	δ_i	DMD mode growth rate
κ	Gladstone–Dale coefficient	ρ	density
ρ_x, ρ_y	normalized density gradient	ρ^*_x, ρ^*_y	density gradient
ϕ_i	DMD eigenvector	ϕ_x, ϕ_y	scaled density gradient

Subscripts, Overlines and Superscripts:

a1–a4	four DMD modes from vertical left cutoff		
b1–b4	four DMD modes from horizontal down cutoff		
h1–h4	four Fourier modes from horizontal down cutoff		
v1–v4	four Fourier modes from vertical left cutoff		
b	background, separation bubble	c	clearance, compensated
p	pure grayscale	r	reference images
$\bar{\cdot}$	temporal or spatial averaging	$\cdot^*$	total or original variables

Accepted to Phys. Fluids 10.1063/5.0147216

I. INTRODUCTION

In most cases, rotor-blade tip clearance is inevitable in ducted turbomachinery (such as rotors of turbines or compressors in aero-engine) to avoid blade-tip abrasion. Figure 1 shows a schematic drawing of a single generic blade contained by a casing wall. Due to the aerodynamic loading, a pressure difference is imposed between the pressure side (PS) and the suction side (SS) of the clearance. This leads to pressure-driven tip leakage flows and related flow–flow interactions, such as the rolling-up of tip leakage vortices (TLVs). TLFs are profoundly important for the performance of rotors because of their significant influence on rotor efficiency loss,[1,2] heat transfer and corrosion fatigue,[3] flow instability[4] and cavitation.[5] The loss introduced by TLFs constitutes about one-third of the total stage loss,[1] and about half of this loss occurs in the gap region.[6] Severe blade tip heat loads are the main cause of turbine blade degradation. This is closely related to tip heat transfer that is very sensitive to the tip flow structures. Research has shown that the blade-tip heat load within a high-pressure turbine varies by up to 50% when switching from sub- to supersonic operating conditions.[7]

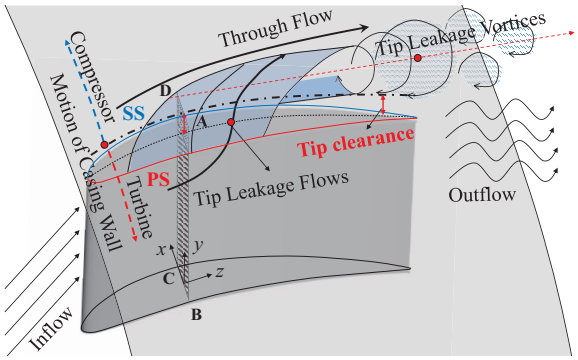

FIG. 1. Schematic view of leakage flows over the blade tip. Tip clearance is the gap between blade tip and the casing wall. Section ABCD indicates a slice along the leakage flow.

The unsteadiness of tip flow structures outside the clearance region (such as the breaking-down of TLVs) has been widely discussed.[8–11] However, the origin of such flow structures is the clearance. Aiming at better understanding the mechanisms of blade tip loss and heat load, TLFs in

the clearance region are to be further discussed. Limited by the narrow space in the tip region, it remains difficult to obtain detailed flow measurements in the clearance. Feng et al.[12] studied the unsteady formation of TLFs in the gap. They observed that the over-tip shock system was established within 0.65s through five stages. In their study, the shock system is dominated by oblique shocks. It becomes relative stable after its quick formation, i.e., no systematical displacement or topology change are observed in it. Hampered by the testing difficulties, very few experimental results for TLFs in the clearance are available in the open literature. These difficulties have been partially overcome by high-fidelity numerical simulations. By direct numerical simulations (DNS), Wheeler and Sandberg[3] observed that TLFs in the clearance are intermittent (neither laminar nor fully turbulent). They also found that the free-stream turbulence intensity is significantly suppressed by the flow acceleration in the clearance. Similar with Feng's observations,[12] the shock system observed in their study is dominated by oblique shocks and is relatively stable upon formation. We observed that the oblique over-tip shock system turned into an unstable shock system when the averaged tip Mach number was reduced to a specific value (Still transonic). We call this state the "critical state", at which the over-tip shocks emerge, travel and decay constantly in the clearance. Figure 2 shows an example of this state. Many aspects of TLF structures and the related motions at the critical state are yet to be clarified.

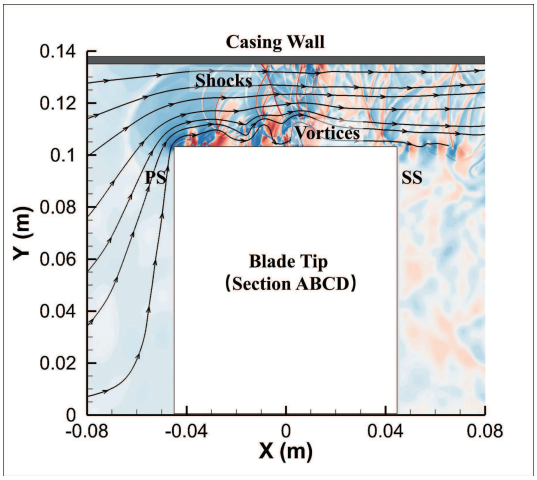

FIG. 2. An example view along section ABCD under transonic condition with an unsteady shock system. TLFs are identified by streamlines and density gradient in the x-direction along section ABCD in Fig. 1.

Flows around ducted rotors are complex, but the TLFs in the clearance can be featured as relatively isolated sub-flow structures bounded by the blade tip and the casing wall. This enables detailed investigations of such flows based on generic wall-bounded blocks with a gap. TLF ranges from subsonic to transonic depends on the clearance size and the imposed pressure difference between the PS and the SS. Highly unsteady over-tip shock waves are expected at the critical state. This may lead to strong interaction between the over-tip shock waves, shear layers and other flow structures. Lock-in effects or coupling effects, such as cavity resonance[13] and vortex induced vibrations,[14] are common in flow interactions. Some kind of lock-in effect is expected in wall-bounded TLFs under the critical state. A possible strong coupling pair is the highly unsteady shock waves and the separated boundary layer. The details of how such flow interactions happens in the clearance region, and how strong they are, are yet to be discussed.

In the past a few years, several flow field visualization techniques, such as oil-film,[15,16] schlieren,[12,17] laser Doppler velocimetry,[18,19] and particle image velocimetry,[20] have been used to study TLFs. The effects of clearance size and tip contouring on the TLF-induced unsteadiness patterns, turbulent kinetic energy, and passage blockage have subsequently been reported. Fischer et al.[21] proposed a frequency-modulated Doppler global velocimetry method to cope with the limited measuring space and high unsteadiness in the tip region. Recently, a time-resolved schlieren visualization technique was used by Feng et al.[12] to investigate the rapid establishment of the in-gap TLF under transonic operating conditions. Time-resolved schlieren visualization can also be used for quantitative analysis through Fourier transforms and dynamic mode decomposition (DMD). These methods have been widely used to analyze wakes[22] and confined gap flows.[23] Rao and Karthick[24] have discussed the influence of image parameters on the DMD of time-resolved schlieren images. These studies provide effective methods for detailed investigations of the TLFs generated by various tip models.

The main objective of this study is to investigate the formation and evolution of over-tip shock waves in the pressure-driven tip leakage flow, resulting in a better understanding of the high unsteadiness of TLFs at the critical state. This goal is achieved by wind-tunnel testing with time-resolved schlieren visualization and image processing, and is supported by additional numerical simulations. Multiple schlieren cutoffs are applied, which enables the quantitative visualization of flow structures in both the horizontal and vertical directions. The experimental configurations are described in Sec. II. The post-processing techniques are presented in Sec. III. In Secs. IV–VI, the results are analyzed and discussed. A simplified model for the prediction of over-tip shock waves

is proposed in Sec. IV. The lock-in effect of over-tip shock waves is discussed in Sec. V. The life cycle of the over-tip shock waves is illustrated in Sec. VI. Finally, the conclusions to this study are presented in Sec. VII.

II. EXPERIMENTAL AND NUMERICAL CONFIGURATIONS

A. Simplified tip models

Simplified blade tip models with a stationary casing wall are used. The model profile, which is illustrated by section ABCD in Fig. 1, is representative of the transverse section of the tip part of rotor blades. This enables detailed observations of the flow structures in the clearance region.

The reason why this simplification can be made is explained by Fig. 3, in which the internal flow field of the Aechen 1-1/2 turbine rig stage is predicted by solver EuranusTurbo. The inlet boundary condition is set based on the radial distributions of total pressure and total temperature of Gallus' experiments.[25] The outlet boundary is solved by radial equilibrium equation with static pressure $P_{out} = 106000$ Pa at $r = 0.288$ m. The back pressure is lower than the experiment to boost stronger TLFs. A cutting plane is made to show the tip leakage flows across the blade tip. Ignoring the change of blade thickness, a quasi two-dimensional (2D) feature can be established in the clearance. Based on this consideration, several similar simplifications have been applied in

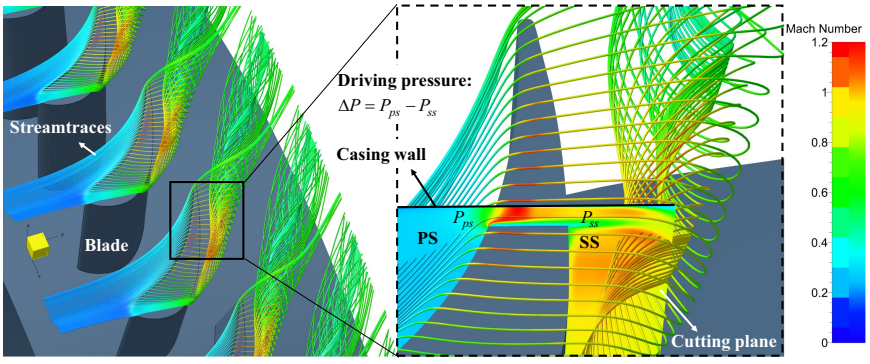

FIG. 3. Tip leakage flows in the Aachen 1-1/2 turbine rig stage with 2 mm tip clearance (solved by Reynolds Averaged Navier-Stokes equations with Spalart-Allmaras turbulence model and enlarged for better view). Cutting plane is flooded with static pressure and the streamtraces are colored by velocity magnitude.

the literature.[3,12,26,27]

In this study, we do not focus on a specific position along the blade chord, because the position of the strongest TLF varies along the chord in different applications. This position tends to be near the leading edge in compressors/fans,[28] at the mid-chord for propeller rotors,[29] and near the mid-to-trailing-edge chord for turbines.[30]

As shown in Fig. 4, the simplified two-dimensional profile was stretched along the depth direction and enlarged to fit into the wind tunnel that has a rectangular working section. The overall

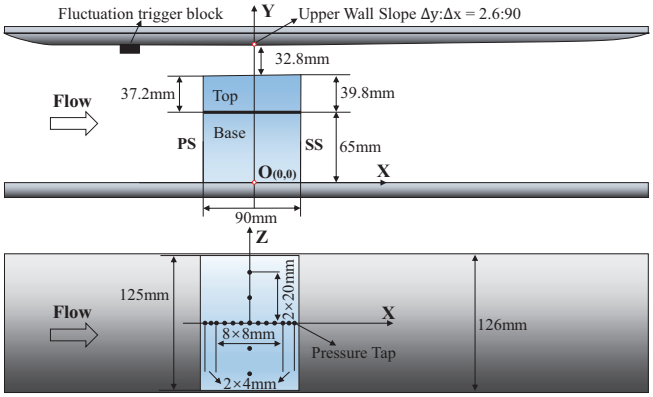

FIG. 4. Schematic view of the model mounted in the wind tunnel, with a frontal view (upper) and top view (lower). The black dots represent the pressure tapping holes. The 13 taps along the X-axis are equally distributed at 8 mm intervals, except for the first and the last three, which have smaller intervals of 4 mm. The five taps along the Z-axis are equally distributed at intervals of 20 mm. A fluctuation triggering block is placed to generate extra flow disturbances for cases discussed in Sec. IV.

model height at the pressure side (PS) is 102.2 mm, which is composed of a 65 mm base and a 37.2 mm top. On the suction side (SS), the top measures 39.8 mm, giving a model height of 104.8 mm at the SS edge (with a height difference of 2.6 mm). This height difference is conformal with the upper wall of the wind tunnel (see subsection II B) to maintain a constant tip clearance. The model width and the tip clearance are 90 mm and 32.8 mm, respectively. This yields a clearance to blade-thickness ratio of 36.44% (2–5% chord), which is within the typical clearance ratio range in fans, compressors, and turbine blades.[6,31] Moore et al.[32] pointed out that the influential area of the core part is limited to twice the tip clearance for transonic TLFs. This value is taken as the criterion for the lower limit. Thus, the present tunnel height to clearance ratio is set to approximately

4.2 at the clearance exit, which is more than twice the core-part size and does not lead to severe tunnel blockage. Seventeen pressure taps are placed on the top surface. Details of the pressure taps are illustrated in Fig. 4. The five taps along the Z-axis are used to monitor the spanwise effect to ensure a two-dimensional flow pattern.

B. Wind tunnel and operating condition

The transonic wind tunnel[17,33] of the Whitehead Aeronautical Laboratory at Queen Mary, University of London, was used for the investigations. Figure 5 shows a photo of the wind tunnel and part of the schlieren system, and a profile with the dimensions of the working section. This is a closed-circuit transonic wind tunnel. The working section used in this study has a width of 126 mm and a height of 135 mm. [The upper wall of the tunnel is slightly divergent in this section, with a slope ratio of about 2.89% (2.6:90), so the model top surface is machined to have a small slope and maintain a constant tip clearance.] The gap between the tip and the upper (casing) wall ranges from 31.3% to 32.1% of the wind tunnel working section height. Steady operation of the wind tunnel is ensured under this clearance ratio. The nominal working Mach number without models ranges from 0–1.4, which enables the generation of transonic flow in the clearance. The small gap between the quartz screen and the model is sealed with a sponge. The small gaps between the tunnel floor and the model parts were sealed with aluminum tape.

The driving pressure, termed the pressure demand (PD), is the pressure supply of the wind tunnel driving system. It ranges from 0 to 827.37 kPa (0–120 psi) for currents tests. The inlet total pressure P^* is measured in the settling chamber immediately before the test section, which has a constant atmospheric pressure. The outlet static pressure P_{out} is measured at the tunnel floor, 350 mm downstream of the model center ($x = 0$ mm), where the static pressure becomes relatively uniform. Consequently, the ratio of pressure difference imposed on the model is defined as $r_p = (P^* - P_{out})/P^*$, which ranges from 0.0–0.297. Applying the simplified tip model at $PD =$ 120 psi, the critical state is achieved when the mean flow in the clearance is accelerated to about $\overline{M}_{max} = 1.2$ near the separation bubble and to $\overline{M}_{e,max} = 0.84$ at the center of the clearance exit. The average Mach number at the clearance exit is $\overline{M}_e = 0.63$. The instantaneous Mach number before shock can be up to $M_{max} = 1.6$. The Reynolds number at the exit of the tip gap [calculated using the clearance and the mass-weighted average speed] is approximately $\mathrm{Re_c} = 3.7 \times 10^5$. The environmental pressure and temperature are relatively stable during the tests. The total temperature

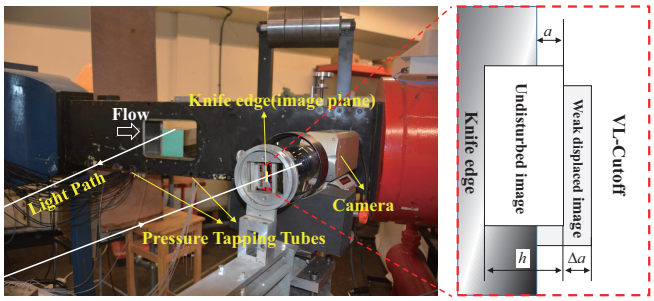

(a) Photo of the wind tunnel.

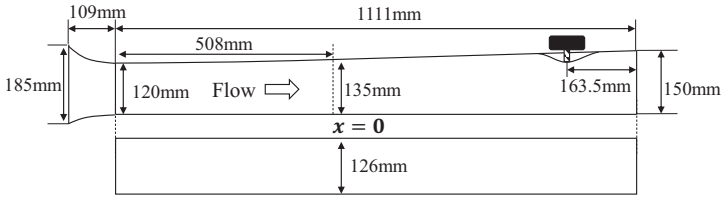

(b) Profile of the wind tunnel.

FIG. 5. Wind tunnel: (a) photo of the closed-circuit transonic wind tunnel with the simplified model and part of the schlieren system (see subsection II C); (b) frontal- and top-view profiles of the wind tunnel.

varies from 290.8–293.3 K. The inlet total pressure is calibrated to be P^* =101.33 kPa at the total temperature of $T^* = 288.15$ K.

C. Time-resolved schlieren visualization system

A symmetric z-type schlieren system was applied in this study (see Fig. 6). Thus, the comma error of schlieren systems is avoided by the symmetry. The component parameters of this system are listed in Table I. The angular deflection of the light ray is linearly proportional to the grayscale captured by a camera that saves the image without gamma correction.[34] Thus, the grayscale measured by the camera, (ϕ_x, ϕ_y), has a linear relationship with the flow density gradient, i.e., $\phi_x = K\partial\rho/\partial x$, $\phi_y = K\partial\rho/\partial y$, where K is a constant determined by the light-source illuminance and parameters of the camera. Assuming the environment refractive index of $n_0 \approx 1$, the flow density gradient is expressed as

$$\frac{\partial\rho(x)}{\partial x} \cong \frac{h[\gamma(x) - a/h]}{\kappa L f_m}, \tag{1}$$

where $\gamma(x)$ is the normalized grayscale. As shown in Fig. 5, $h = 0.3$ mm is the height of the slit light source and a is the passing height of the image at the knife-edge plane. Thus, a/h represents the cutoff ratio. Generally, the value of a varies from $0.2h$–$0.8h$ depending on the camera's need for proper exposure and the balance between the schlieren sensitivity and the measuring range. The length of the schlieren extent is $L = 126$ mm (width of the wind tunnel). The focal length of the mirror is $f_m = 1828.8$ mm, and the Gladstone–Dale coefficient is $\kappa \approx 0.23$ cm$^3\cdot$ g^{-1}.

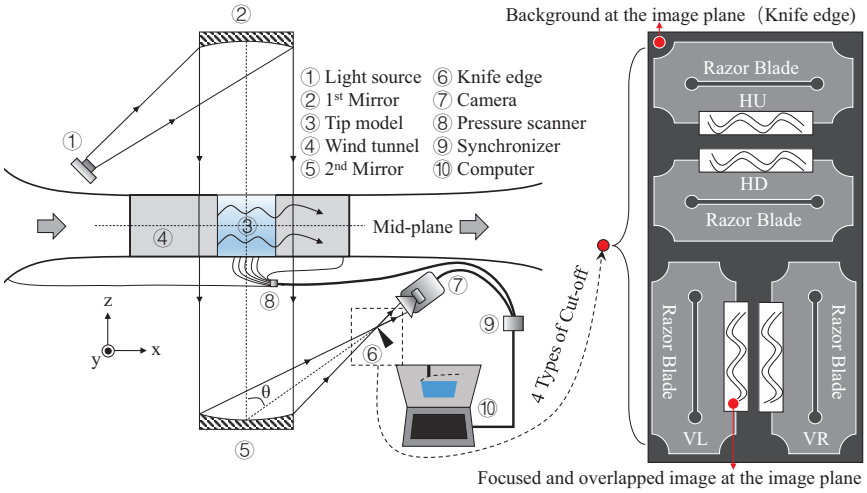

FIG. 6. Schematic drawing of the symmetric z-type schlieren and pressure testing system.

TABLE I. Parameters of the schlieren components.

Light Source	KEYMED slit source		Slit height	0.3 mm
Mirrors	Focus	1828.8 mm	Diameter	203.2 mm
Knife edge	Razor blade		Extent Length	126 mm
Lens	55-80 mm			
	Model	Phantom V4.3	Sample rate	8510 Hz
Camera	Exposure	10 μs	Sample time	1.888 s
	Resolution (pixels)		512 × 128	

The application of a cutoff is essential for schlieren measurements. The cutoff type denotes the direction from which the slit light at the knife-edge plane is partly blocked, as shown in Fig. 6. Four

types of schlieren cutoffs are used. They are the vertical-left (VL), vertical-right (VR), horizontal-down (HD), and horizontal-up (HU) cutoffs. The schlieren cutoff works as follows: if the axis is set pointing to the outer-normal direction of the knife-edge, the light is deflected to the knife-edge and is blocked at the presence of negative density gradient, resulting in low grayscale in the image and vice versa. The slit light source and the edge of the razor blade are placed vertically or horizontally according to the vertical- or horizontal-cutoff types. Multiple cutoff directions of a schlieren system are necessary for quantitative measurements, though only one cutoff direction is used[12,35] when forming a qualitative visualization of the flow. This is important because the sensitivity and the effective measuring range of a schlieren system are controversial.[36] To extend the effective measuring range, a superposition technique is applied. The cutoff ratio $\eta = (h-a)/h$ varies within a range of $[20\%, 80\%]$ in the experiments. The superposition of two images measured by two cutoffs in opposite directions is used to achieve a larger measuring range.

TABLE II. Relationships between cutoff type and flow structures that can be revealed by schlieren patterns in compressible flows (verified in subsection III B).

Cutoff	Good at capturing	Possible flow structures revealed
VL	$\partial\rho/\partial x > 0$	Shocks, vortex–shock interaction
VR	$\partial\rho/\partial x < 0$	Expansion wave, separation bubble
HD	$\partial\rho/\partial y > 0$	Separation bubble, vortex shedding
HU	$\partial\rho/\partial y < 0$	Separation bubble, vortex shedding

The flow patterns revealed by schlieren images are essentially the flow compression or expansion in the x- or y-direction. Flow structures such as shock waves, separation bubbles, expansion waves, and shear layers are accompanied by strong density gradients. Thus, the schlieren patterns in turn reveal such flow structures. According to preliminary knowledge about TLFs,[32] the mappings between the schlieren cutoff type and the revealed flow structures are listed in Table II (Numerical simulations in subsection III B are performed to verify such statements.). The flow structures that exhibit an abrupt density increase near the upper wall can be identified as shock waves. Abrupt density changes near the pressure side edge are identified as the boundaries of separation bubbles. Strong density gradients in the y-direction denote the core-trajectory of vortex shedding. The periodic shedding of negative–positive density gradient patches in the x-direction

is identified as vortex shedding, and these negative–positive density gradient zones along the core-trajectory are identified as vortices.

III. IMAGE POSTPROCESSING AND FLOW STRUCTURE IDENTIFICATION

A. Postprocessing of schlieren images

The image postprocessing tasks include averaging, cropping, resizing, and compensating. First, the averaged images are generated from the raw images in grayscale, calculated by $\bar{g}(i,j) = \sum_{n=1}^{n_p} g_n(i,j)/n_p$, where $g(i,j)$ is the grayscale at pixel index (i,j) and n_p =16 064 is the number of images sampled in a period of 1.888 s at 8510 images per second. Second, the images are cropped and resized. Third, image compensation is applied to improve the accuracy. The compensated grayscale g_c is calculated from the original grayscale g by

$$g_c = (g - g_b)\frac{\bar{g}_r - g_{r,b}}{g_r - g_{r,b}}, \tag{2}$$

where g_b, g_r, $\bar{g}_r$, $g_{r,b}$ are the grayscale of the background (grayscale measured at the solid model), reference (measured without flow), averaged reference, and reference background, respectively. Examples of the compensated unsteady images are displayed in Figs. 7(a) (Multimedia view) and 7(c) (Multimedia view). The averaged images are displayed in Figs. 7(b) and 7(d).

The averaged pure reference grayscale $\bar{g}_{r,p} = \bar{g}_r - g_{r,b}$ is subtracted from the compensated grayscale to obtain a new variable. Due to the linear relationship between the grayscale and the density gradient in the x- or y-direction, this new variable is termed the scaled density gradient, $K_{sv}\rho_x^*$ or $K_{sh}\rho_y^*$. It is calculated as $K_{sv}\rho_x^* = g_c - \bar{g}_{r,p}$ in the case of vertical cutoff and $K_{sh}\rho_y^* = g_c - \bar{g}_{r,p}$ in the case of horizontal cutoff, where K_{sv} and K_{sh} are the coefficients of the schlieren system in the case of vertical and horizontal cutoffs, respectively. The images are saved with 8-bit unsigned integers (uint8, 0–255); thus, the accuracy is limited to $\pm K_{sv} max(|\rho_x^*|)/256$ or $\pm K_{sh}|max(\rho_y^*)|/256$. Theoretically, if the properties of the light source and the cutoff ratio remain unchanged, the coefficients K_{sv} and K_{sh} should be the same for all cases. However, they are not exactly equal because the dimensions of the light source change slightly when switching from vertical to horizontal cutoff, and the cutoff ratio is adjusted to give a better view. However, the assertion $K_{sv} \approx CK_{sh}$ is valid, where C is a case-sensitive constant. To eliminate this difference, the density gradients in both directions are normalized based on the maximum value, and the result is recorded as the dimensionless density gradients ρ_x and ρ_y.

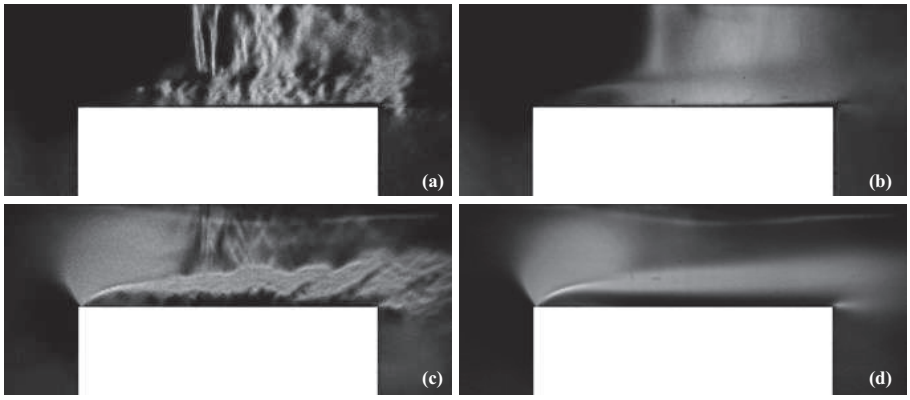

FIG. 7. Compensated unsteady (g_c) and averaged ($\bar{g_c}$) grayscale images of the simplified model in the cases of VL- and HD-cutoffs at $r_p = 0.297$ (PD120): (a) unsteady view of VL-cutoff (Multimedia view); (b) averaged view of VL-cutoff; (c) unsteady view of HD-cutoff (Multimedia view); (d) averaged view of HD-cutoff. Slope of the model top surface is omitted.

Limited by the measuring range of the schlieren system, some areas in the sampled images may exceed the measuring range and become invalid, such as the lower-bound areas in the VL- and HD-cutoff cases or the upper-bound areas in the VR- and HU-cutoff cases. The measuring zone, Ω, is composed of the valid zone, Ω_v, and the invalid zone, Ω_i. Thus, $\Omega = \Omega_v \cup \Omega_i$. The validity is determined by the measuring range of the schlieren system. The zone is labeled "invalid" when the grayscale distribution in this region reduces to the lower limit (the background grayscale) or increase to the upper limit. In the invalid zone, the grayscale distribution becomes locally constant, losing the details of flow structures. Fortunately, results from two parallel cutoff-types (VL- and VR-cutoff, or HD- and HU-cutoff) are complementary. Thus, the cases of parallel cutoff-types form a pair. The valid zones of pair cases satisfy the following relation

$$\begin{aligned} &\Omega_v' = \Omega_{v,VL} \cup \Omega_{v,VR} = \Omega_{v,HD} \cup \Omega_{v,HD} = \Omega_v \cup \Omega_i, \\ &\Omega_{v,VL} \cap \Omega_{v,VR} \neq \emptyset,\ \Omega_{v,HD} \cap \Omega_{v,HD} \neq \emptyset. \end{aligned} \tag{3}$$

where Ω_v' is the whole measuring zone without invalid patches, the subscript VL, VR, HD or HU denotes results from corresponding cutoff case. Thus, it is able to remove the invalid region of each single-cutoff case by superposing results from the case from the paired case. There exists an overlapped region, $\Omega_{v,VL} \cap \Omega_{v,VR}$ or $\Omega_{v,HD} \cap \Omega_{v,HU}$, in which results from both cases should be

valid. A simple averaging step is performed in this area to avoid discrepancies. Thus, the density gradient in the x-direction is expressed as

$$\begin{cases} \rho_x(\mathbf{X},t) = \rho_{x,VL}(\mathbf{X},t),\ \mathbf{X} \in \Omega_{v,VL} - \Omega_{v,VL} \cap \Omega_{v,VR}, \\ \rho_x(\mathbf{X},t) = \rho_{x,VR}(\mathbf{X},t),\ \mathbf{X} \in \Omega_{v,VR} - \Omega_{v,VL} \cap \Omega_{v,VR}, \\ \rho_x(\mathbf{X},t) = [\rho_{x,VL}(\mathbf{X},t) + \rho_{x,VR}(\mathbf{X},t)]/2,\ \mathbf{X} \in \Omega_{v,VL} \cap \Omega_{v,VR}. \end{cases} \tag{4}$$

Similarly, the density gradient in the y-direction is written as

$$\begin{cases} \rho_y(\mathbf{X},t) = \rho_{y,HD}(\mathbf{X},t),\ \mathbf{X} \in \Omega_{v,HD} - \Omega_{v,HD} \cap \Omega_{v,HU} \\ \rho_y(\mathbf{X},t) = \rho_{y,HU}(\mathbf{X},t),\ \mathbf{X} \in \Omega_{v,HU} - \Omega_{v,HD} \cap \Omega_{v,HU} \\ \rho_y(\mathbf{X},t) = [\rho_{y,HD}(\mathbf{X},t) + \rho_{y,HU}(\mathbf{X},t)]/2,\ \mathbf{X} \in \Omega_{v,HD} \cap \Omega_{v,HU}. \end{cases} \tag{5}$$

The time-domain superposing in Equ. (4-5) is valid only if the measurements of the cutoff-pair are performed simultaneously. However, the measurements are usually performed subsequently under similar operating conditions. In this case, one can perform Fourier transform to accomplish the superposing in the frequency domain to get $\tilde{\rho}_x(\mathbf{X},\omega)$ and $\tilde{\rho}_y(\mathbf{X},\omega)$. The simple averaging in the overlapped region is also valid by ignoring possible phase difference. Or else, one can perform time-averaging to get $\overline{\rho}_x(\mathbf{X})$ and $\overline{\rho}_y(\mathbf{X})$.

Taking the time-averaged density gradient as an example, as shown in Fig. 8, each of these invalid areas is marked by a circled cross. To remove the invalid areas, the overall field of the density gradient is regenerated by the superposition of the VL- and VR-cutoff cases for $\overline{\rho}_x(\mathbf{X})$, and by the superposition of the HD- and HU-cutoff cases for $\overline{\rho}_y(\mathbf{X})$. The density gradients in the invalid areas are replaced by the value from the opposite cutoff type. For instance, the invalid area of the VL-cutoff case [see Fig. 8(a)] is replaced by that of the VR-cutoff case [see Fig. 8(b)]. The average value of these two cases is adopted in the contact area. Thus, the VL- and VR-cutoff cases collapse into the vertical cutoff case, and the HD- and HU-cutoffs turn into the horizontal cutoff case. The time-averaged field is displayed in Fig. 9. The superposing of the cutoff-pair yields the overall distribution of density gradient in the clearance, resulting in the identification of the separation bubble [Label A in Fig. 9(a-b)], the shock waves [Label B in Fig. 9(a)], several compression region [Label C and D in Fig. 9(a)], and the trajectory of vortex-core [The streak after label A in Fig. 9(b)].

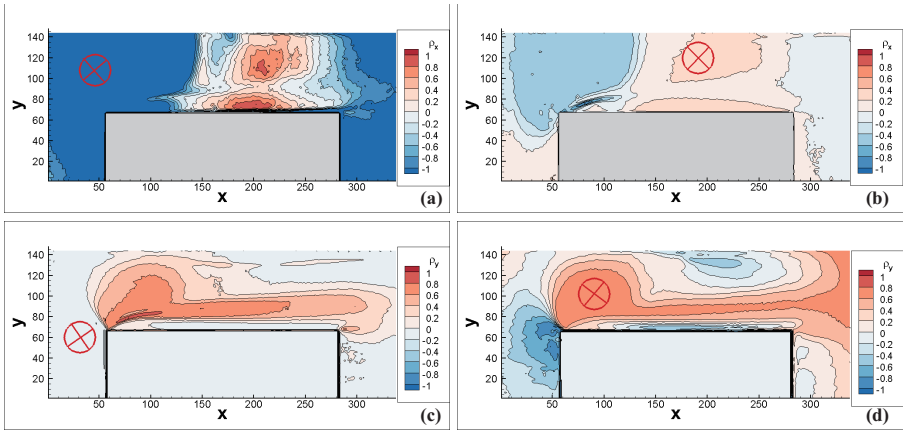

FIG. 8. Averaged density gradient from four cutoff cases at $r_p = 0.297$ (PD120) with coordinates in pixels. The invalid region is marked by a circled cross: (a) VL-cutoff; (b) VR-cutoff; (c) HD-cutoff; (d) HU-cutoff.

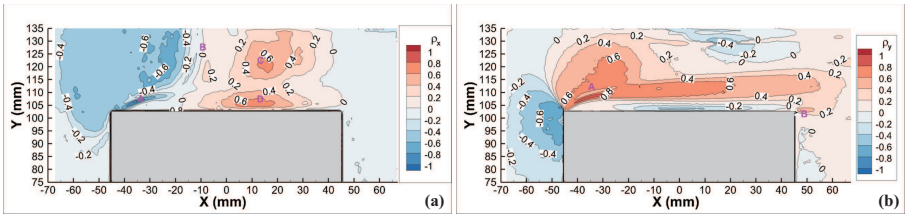

FIG. 9. Mean density gradient $(\overline{\rho}_x, \overline{\rho}_y)$: (a) measured $\overline{\rho}_x$; (b) measured $\overline{\rho}_y$. Maximum values are selected to normalize the density gradient based on the measurement in case PD120 ($r_p = 0.297$). The vertical and horizontal cases are normalized independently.

B. Verification of schlieren-observed flow structures

The relation list in Table II is an assertion to be verified by additional numerical simulations. The goal of such simulations is to qualitatively prove that the observed flow structures are what we expected (shocks, vortex shedding or shear-layer flapping) instead of other flow structures. Therefore, the numerical resolution is designed aiming at this target. Moreover, the flow is assumed to be uniform along the span, thus, two-dimensional (2D) simulations are performed.

The IDDES model[37,38] is applied under the finite volume framework with unstructured mesh.

Details of this model is given in Appendix Sec. VII, in which the model equations, turbulence models and corresponding coefficients are given. Second order finite volume method is applied with the gradients reconstructed by a compact least-squares method.[39] The fluxes are treated by Roe's approximate Riemann solver for the inviscid terms and by direct discontinuous Galerkin (DDG) method[40] for the viscous terms. Spatial discretization is performed by second-order upwind scheme. Time-marching is achieved by dual-time stepping. Following the physical flow domain in the experiment, the computational domain is set as illustrated in Fig. 10. It extends from $x = -0.164$ m ($5c$ upstream the model) to $x = 0.426$ m ($13c$ downstream), and the model is centered at $x = 0$ m (model center, see Fig. 4). Two grid nodes are applied to the span. The reference pressure tap is set at $x = 0.35$ m ($9.3c$ downstream). Thus, the outlet condition is adjusted to match the pressure at the reference tapping position with that measured from the experiment.

Non-reflection characteristic inlet and outlet boundary conditions are applied. We assume the

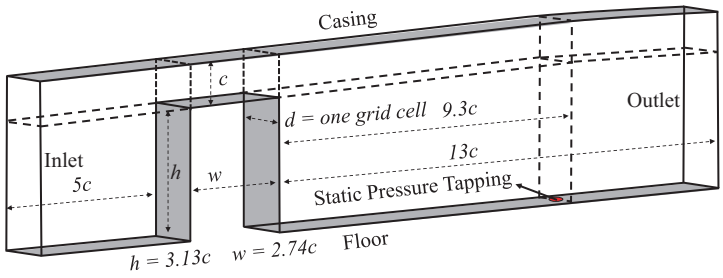

FIG. 10. The computational domain. No-slip wall boundary conditions are applied on the floor, the blade tip and the casing. The pressure outlet boundary is set at $13c$ downstream the model.

turbulence is fully developed in the tunnel. So, the in-coming turbulence intensity and length scale are evaluated by

$$I = \frac{u'}{u_{avg}} \approx 0.16 Re_{tunnel}^{-\frac{1}{8}}, \quad l_{turb} \approx \frac{0.07H}{C_\mu^{3/4}},$$

where $C_\mu = 0.09$ is a parameter that is consistent with C_μ as used in the $k-\varepsilon$ model. Thus, a mild in-flow turbulence is applied to be 3.2% with a length scale of $l_{turb} = 57.5$ mm.

The results of grid sensitivity tests and flow validation are displayed in Fig. 11. The time-averaged pressure distribution is in good agreement with the test data when the clearance grid is finer than $n_c \times n_w \times n_d = 800 \times 3200 \times 2$. Thus, the mesh in the gap region is set to $n_c \times n_w \times n_d = 800 \times 3200 \times 2$. Mesh details in the start region of the PS-side separation bubble are illustrated in

Fig. 12. A subsonic case, $r_p = 0.166$ (PD80, $M_{max} < 1.0$, $\overline{M}_e = 0.51$, $\mathrm{Re_c} = 3.2 \times 10^5$), is displayed as a reference. The instantaneous vorticity magnitude is shown as an indicator of the boundary of the separation bubble started from the PS-edge. The mesh is fine enough to resolve the separation

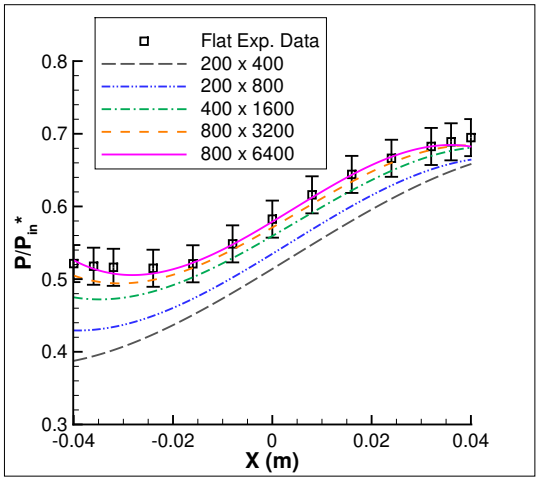

FIG. 11. Comparisons of the predicted and measured static pressure distributions (time-averaged) at the tip surface at $r_p = 0.297$ (PD120). Five sets of clearance grids were tested.

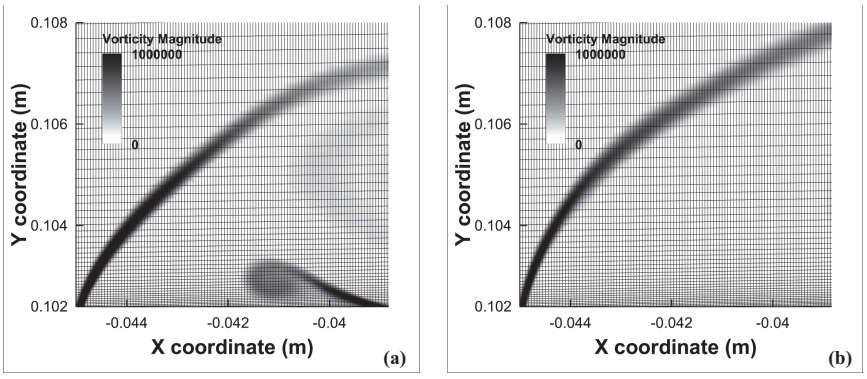

FIG. 12. Computational mesh in the start region of the PS-side separation bubble, showing every fourth grid line. Instantaneous vorticity magnitude is displayed: (a) vorticity magnitude at $r_p = 0.166$ (PD80); (b) vorticity magnitude at $r_p = 0.297$ (PD120).

bubble. The height of this separation bubble is suppressed under the transonic condition. The final mesh has a dimensionless scale of $Y^+ \approx 1$ and $X^+ \approx 28$ (Based on Reynolds number $\mathrm{Re_c}$, which is calculated by the clearance and averaged flow speed at the exit of the clearance), resulting in a total grid cells of about 4.4 million. Based on this grid configuration, the timestep is set to be 2×10^{-7} s.

Figure 13(a) displays four time steps of the unsteady flow measured with the vertical cutoff at $r_p = 0.297$ (PD120, $\overline{M}_e = 0.63$). In the region labeled ③, several vertical-line structures are present with their motions marked by dashed lines. These structures are verified to be shock waves using the IDDES simulations, as compared with Fig. 13(b). At timestep T1, unstable shock waves are generated in the compression region behind the third shock, labeled ⓪. As the shock wave grows stronger, it propagates upstream with decreasing strength and travel speed. This process

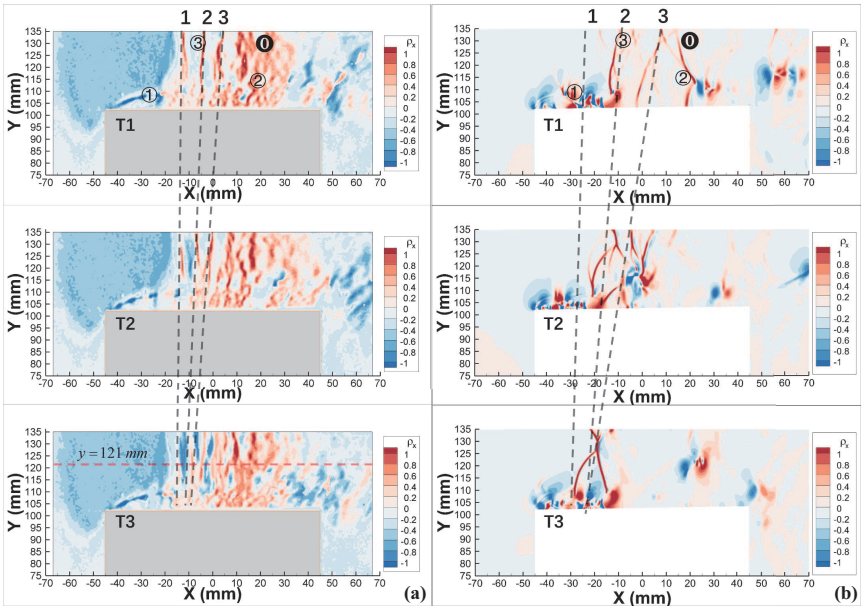

FIG. 13. Time-resolved density gradient distributions at $r_p = 0.297$ (PD120): (a) measured ρ_x; (b) predicted ρ_x. Shock motions are indicated by dashed lines. Starting time T1 is a time anchor. Aiming at identifying the classification of flow structures, the starting time T1 is not necessary to be the same for the simulation and the experiment. Time interval in both cases is $\delta t = 1/8510$ s.

continues until it stops moving and gradually fades out when reaching the upstream limit, as marked by the first dashed line. A separation bubble labeled ① is formed near the pressure-side edge. The low-high-paired pattern at the boundary of the bubble indicates the vortex shedding that generates the main shear-layer flapping. The shear layer wraps around the separation bubble. The periodic vortex shedding and the resulting shear layer flapping are the main driving forces for the unsteadiness of the shock waves. This process is more clearly captured by the footprints along the line $y = 121$ mm, as plotted in Fig. 14. Each of the first few spikes indicates a shock wave. These shock waves are generated in the region enclosed by the rectangular box where grayscale spikes start to emerge. After their formation, the shock waves travel upstream and gradually fade out until they vanish at the upstream limit.

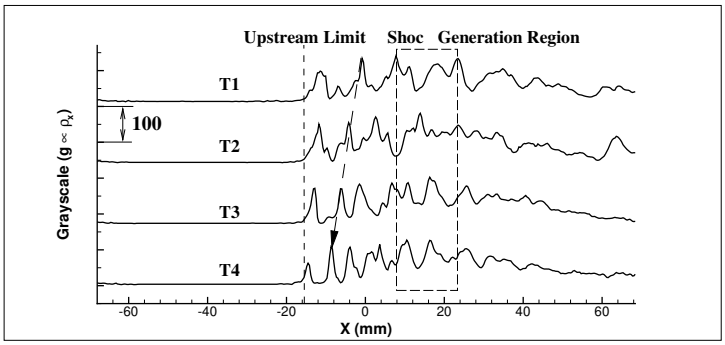

FIG. 14. Measured grayscale along line $y = 121$ mm [see Fig. 13(a)-T3] with VL-cutoff at $r_p = 0.297$ (PD120). Curves are evenly redistributed in the vertical direction with an increment of 170. Timesteps T1–T3 are the same as in Fig. 13(a).

The horizontal flow structures are captured by the horizontal schlieren-cutoff. As shown in Fig. 15, flapping motions of the flow structures labeled ② can be observed. These structures are verified by the IDDES results to be vortex shedding and the over-tip shear layer and the trajectory of vortex shedding. Thus, flow structure ② reveals the footprints of vortex shedding, and it contains a series of vortices shed from the PS-edge. Additionally, a smaller vortex shedding footprint labeled ⑥ is generated from the suction-side edge. The flapping of the shear layer is clearly revealed by the footprints along the line $x = 0$ mm plotted in Fig. 16. The high platforms indicate the density recovery from the vortex core. The upper boundary is closely related to the shear layer of V_x, and the lower boundary of these high platforms is composed of the loci of vortex cores. The

Accepted to Phys. Fluids 10.1063/5.0147216

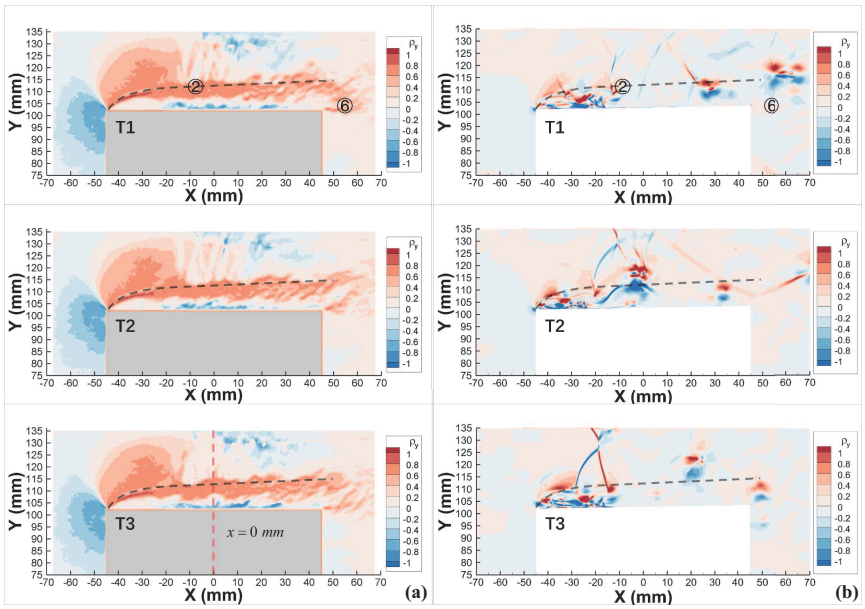

FIG. 15. Time-resolved density gradient distributions at $r_p = 0.297$ (PD120): (a) measured ρ_y; (b) predicted ρ_y. The time interval in both cases is $\delta t = 1/8510$ s.

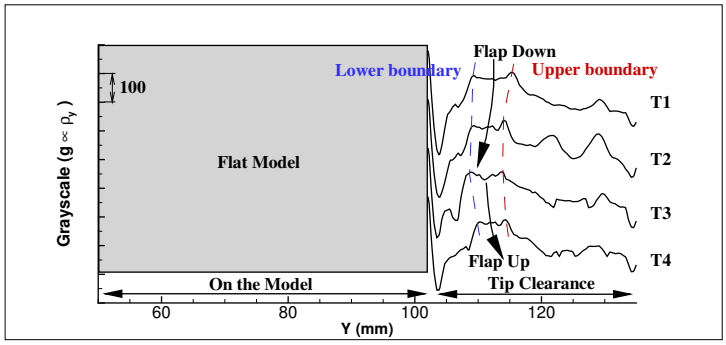

FIG. 16. Measured grayscale, $g \propto \rho_y$, along the line $x = 0$ mm [see Fig. 15(a)-T3] with VL-cutoff at $r_p = 0.297$ (PD120). T1–T3 are the same as in Fig. 15(a).

shear layer and vortex train are observed to flap up and down.

IV. DISTRIBUTION OF OVER-TIP SHOCKS AND A SIMPLIFIED PREDICTION MODEL

We focus on the transonic case, $r_p = 0.297$ (PD120, critical state, $M_{max} = 1.6$, $\overline{M}_e = 0.63$, $\mathrm{Re_c} = 3.7 \times 10^5$). Looking back at Fig. 14, one observes that the over-tip shocks exist in the form of a dynamic shock system instead of a single shock cell. Unlike the shock system under supersonic conditions, this shock system is highly unstable. This is revealed by the global movement and the locally oscillation of shock waves at the same time. The over-tip shock system are composed of a series of up-propagating near-normal shocks. Such motion of shock system reminds us the evolution of repeated sawtooth waves. Based on the assumption of sawtooth waves and the weak shock theory, a simplified model is proposed to describe the distribution of over-tip shocks.

Before describing the model, the density gradient, ρ_x, measured by the schlieren is related to the strength of shocks, Π, by the following expression.

$$\Pi = \frac{A_1\rho_x^2 + A_2\rho_x + A_3\sqrt{(A_4-\rho_x)\rho_x}}{(\rho_x + A_5)^2}. \tag{6}$$

This equation is derived in the Appendix Sec. VII, and the coefficients are evaluated to be, $A_1 = -7$, $A_2 = 592702703$, $A_3 = 331330883$, $A_4 = 76204633$, $A_5 = -63503861$, at the condition with parameters: $\nu = 1.48 \times 10^{-5}\, m^2 \cdot s^{-1}$, $a_0 = 340\, m \cdot s^{-1}$, $\rho_1 = 1.29\, kg \cdot m^{-3}$. Plotting Equ.(6) as Fig. 17, one can find that the shock strength is almost linearly proportional to the density gradient in the range of $[5000, 1 \times 10^7]\, kg \cdot m^{-4}$, which covers the shock strength $\Pi \in [0.05, 4.8]$. This range is able to cover the shock strength discussed in this article (Fig. 18). Therefore, the density gradient measured by schlieren holds a quasi-linear relation with the strength of shock waves. This makes it possible to discuss the evolution of over-tip shock waves by the results from the schlieren.

Assume the over-tip shock waves form a shock system described by repeated sawtooth wave and the shock system as a whole travels at the speed of sound in undisturbed fluid, thus, the shock strength is a function of travel time that can be expressed as

$$\Pi = \left[\frac{1}{\Pi_0} + \frac{a_0 t}{\lambda} \cdot \frac{\gamma+1}{2\gamma}\right]^{-1}, \tag{7}$$

where a_0 is the background sound velocity, γ is the specific heat ratio, λ is the wave length of the repeated sawtooth wave.[41] For current flow configuration, the shock waves propagate along the reversed direction of the x-axis. Thus, the travel distance of shock front from the initial position is written as

$$x_0 - x_s = \int_0^t (M_s - M_f) a_0 dt, \tag{8}$$

Accepted to Phys. Fluids 10.1063/5.0147216

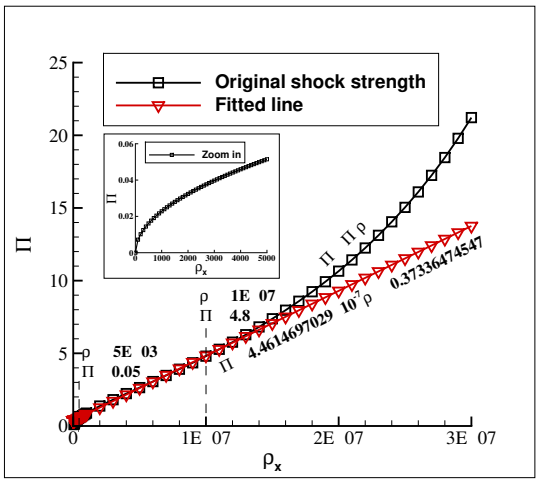

FIG. 17. Relation between the density gradient, ρ_x, and the shock strength Π.

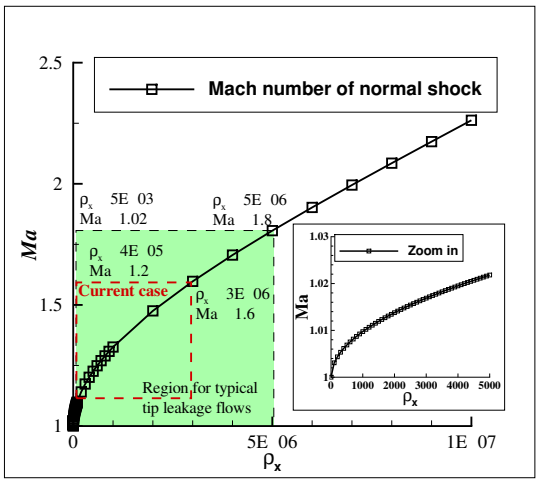

FIG. 18. Relation between the Mach number, Ma, and the density gradient ρ_x of a normal shock. For current transonic case, the $Ma \in [1.02, 1.6]$. The plot for very weak shock is enlarged in the sub-figure.

where x_0 and x_s are the initial and current shock positions, respectively. M_s is the Mach number of

the shock front expressed as a function of the shock strength Π, which is written as

$$M_s = \sqrt{1 + \frac{\gamma+1}{2\gamma}\Pi}, \tag{9}$$

and M_f is the Mach number of fluid expressed as

$$M_f = \bar{M} + \sum_{i=1}^{n} c_i cos(2\pi f_i t), \tag{10}$$

in which $\bar{M}$ is the mean flow Mach number and the summation term indicates the velocity fluctuations with frequency f_i and amplitude c_i. Substitute Equ. (7), Equ. (9) and Equ. (10) to Equ. (8), and let $x_s' = x_0 - x_s$, $K = 2\gamma/(\gamma+1)$, the travel distance can be derived from the integration as

$$x_s' = -\lambda ln\frac{\lambda}{\lambda + a_0\Pi_0 Kt} + (1-\bar{M})a_0 t - a_0\sum_{i=1}^{n}\frac{c_i sin(2\pi f_i t)}{2\pi f_i}. \tag{11}$$

The travel time is also a function of the shock strength. Thus,

$$t = \frac{\lambda}{a_0 K}\left(\frac{1}{\Pi} - \frac{1}{\Pi_0}\right). \tag{12}$$

Substitute Equ. (12) to Equ. (11), one can get the shock travel distance expressed as

$$x_s' = \underbrace{-\lambda ln\frac{\Pi}{\Pi_0}}_{\text{Initial shock state, } x_{si}} + \underbrace{\frac{(1-\bar{M})}{K}\lambda\left(\frac{1}{\Pi} - \frac{1}{\Pi_0}\right)}_{\text{Mean background flow, } x_{sm}} \underbrace{-\frac{a_0}{2\pi}\sum_{i=1}^{n}\frac{c_i}{f_i}sin\left[\frac{2\pi f_i\lambda}{a_0 K}\left(\frac{1}{\Pi} - \frac{1}{\Pi_0}\right)\right]}_{\text{Background flow fluctuations, } x_{sf}}. \tag{13}$$

The movement of shocks is driven by three factors, the initial shock state, x_{si}, the mean background flow, x_{sm} and the background flow fluctuations, x_{sf}. The background flow fluctuations are also a driving force for the over-tip shock oscillations. The term, x_{sf}, is self-eliminated at full cycles and the term c_i/f_i is observed to be small. Therefore, this term can be omitted if the shock is not very weak, then, one can find a linear relation between shock position and the wave length of the saw-tooth wave. In practice, the sawtooth wave is irregular and shock merging happens when weaker shock is overtaken by stronger one. At the merging point, the strength and wavelength of two N-shape waves are superposed. Assume shock overtaking occurs at a constant rate. Thus, the superposing process allows us to describe it by linearly growing wavelength, $\lambda = \lambda_0 + Ax_s'$, and linearly growing shock strength $\Pi_0 = \Pi_{00} + Bx_s'$ (λ_0 and Π_{00} are the initial state of the sawtooth wave, A and B are two empirical constants to be determined by the testing data, for current case, $A \approx 1.0$ and $B \approx 500$.).

To validate this model, schlieren data along line $y = 128$ mm are extracted and superposed by 16043 time steps. The superposed dark-dot cluster in Figure 19 reveals the overall strength

evolution of the over-tip shock waves (calculated from the observed density gradient). Thus, the envelope curve, fitted from the top-ten samples at each position, is a proper description of the movement of over-tip shock waves. It shows that the shock strength satisfies a tooth-like distribution. Centered at the peak position (set the peak position as the initial/reference state), we find that both the generation and the decaying branches satisfy a logarithmic function with the travel distance of over-tip shock waves. For the generation branch, $\Pi \approx -0.286\ln(-\mathrm{x}_s') + 1.069$, if $x_s' < 0$, and $\Pi \approx 0.181\ln(\Delta\mathrm{x} - \mathrm{x}_s') + 0.096$, if $x_s' \geq 0$ for the decaying branch. Averaged through timesteps, the initial wave length, initial/reference shock strength (peak strength) and background Mach number are $\lambda_0 = 0.008$ m, $\Pi_{00} = 0.8$ and $\bar{M} = 1.2$, respectively. The first two flow fluctuations have amplitudes and frequencies of $(c_1, c_2) = (0.1, 0.05)$ and $(f_1, f_2) = (960\ \mathrm{Hz}, 2480\ \mathrm{Hz})$. The prediction agrees well with the experiment when shock strength is greater than $\Pi = 0.2$. The vast deviation for $\Pi < 0.2$ is because the shock overtaking and merging occurs frequently near the upstream limit of shock propagation, the linear superposing model fails in this region. The proposed model is not aimed for the prediction of the generation branch, nevertheless, the left-branch predicted by the contribution of background flow, $x_{sm} + x_{sf}$, agree quite well with the data. This

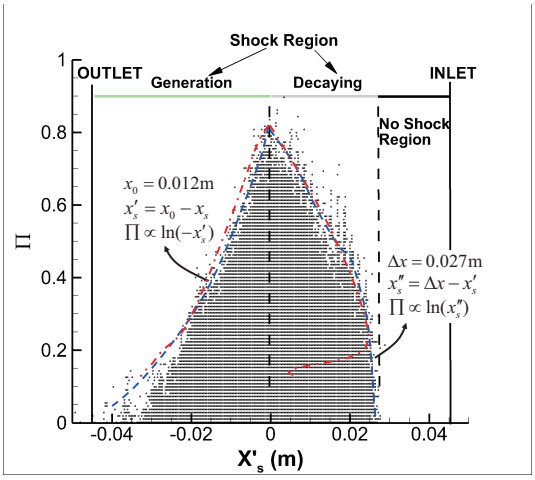

FIG. 19. Case with normal inflow fluctuations: Superposed Π-x_s' plotting (dark dot cluster), its envelop curves (blue dashed line) and the predicted curves (red dash-dotted line, left branch by $x_{sm} + x_{sf}$ and right branch by x_s'). The peak is translated to be $x_s' = 0$. $\Delta x = 0.027$ m is the distance between the upstream limit and the peak position of the over-tip shocks (distance between two dark vertical dashed lines).

implies that the background flow effects may dominate the shock generation process.

This model is further applied to over-tip shock prediction under larger background flow fluctuations. As shown in Fig. 4, for this case, a block is placed upstream the clearance inlet. The block has 5.33 mm in height, 17 mm in width and was placed 70 mm upstream of the clearance inlet. As a result, additional flow fluctuations are generated as $(c_3, f_3) = (0.03, 1026\text{Hz})$. This has great impact on the evolution of over-tip shock waves. Figure 20 shows that this additional flow fluctuation postpones the emerge of shock peak from $x_0 = 0.012$ m to $x_0 = 0.003$ m, the upstream propagating distance is also reduced from $\Delta x = 0.027$ m to $\Delta x = 0.019$ m. Applying the proposed model to this case, good agreement is achieved for the shock decaying branch; while the left branch starts to deviate from prediction because the shock generation process is significantly disturbed by upstream fluctuations. Predicted distributions of shock strength are plotted in Fig. 21. The overall propagation distance x_s' is split into three contributions that represent three mechanisms of over-tip shock dynamics. For both the normal-fluctuation and the extra-fluctuation cases, the initial shock state (dashed green line) dominates the shock motions. The related curve satisfies an exponentially decaying law, $\Pi_i = \Pi_0 e^{-x_{si}/\lambda}$. When the shocks decay to be weaker than 0.2, the

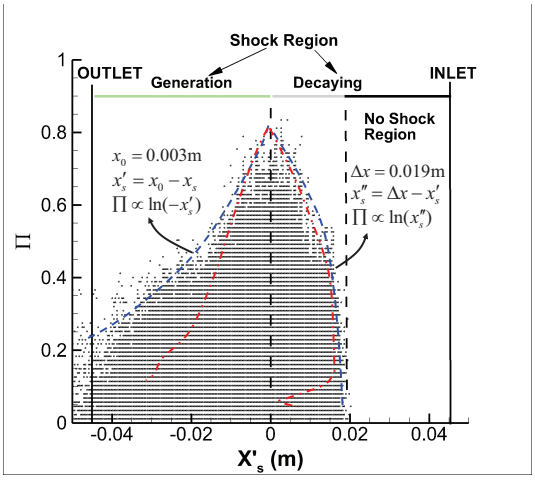

FIG. 20. Case with additional inflow fluctuations: Superposed Π-x_s' plotting (dark dot cluster), its envelop curves (blue dashed line) and the predicted curves (red dash-dotted line, left branch by $x_{sm} + x_{sf}$ and right branch by x_s'). The peak is translated to be $x_s' = 0$. $\Delta x = 0.019$ m is the distance between the upstream limit and the peak position of the over-tip shocks (distance between two dark vertical dashed lines).

Accepted to Phys. Fluids 10.1063/5.0147216

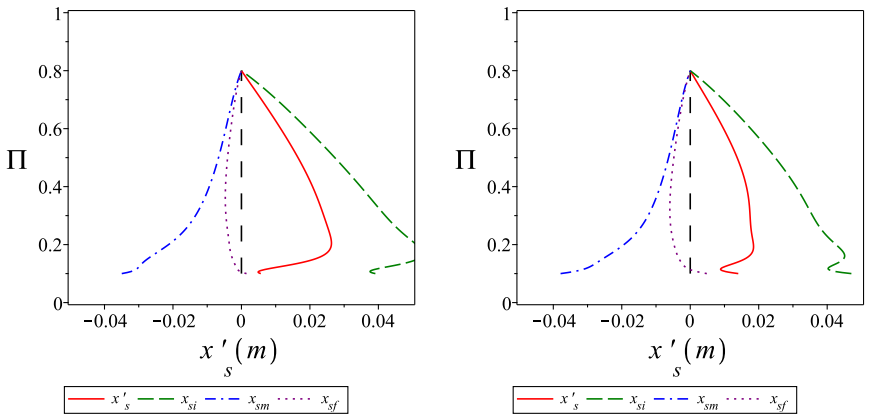

(a) Normal flow fluctuations. (b) Extra flow fluctuations.

FIG. 21. Relationship between the shock position x_s' and shock strength Π. The shock position involves contributions from the initial state x_{si}, the mean background flow x_{sm} and the background flow fluctuations x_{sf}. (a): Fluctuations $(c_1 = 0.1, f_1 = 960\ Hz), (c_2 = 0.05, f_2 = 2480\ Hz)$; (b) Fluctuations $(c_1 = 0.1, f_1 = 960\ Hz), (c_2 = 0.05, f_2 = 2480\ Hz), (c_3 = 0.03, f_3 = 1026\ Hz)$.

background flow (dash-dotted blue line) takes control of the shock motions. The related curve satisfies an inversely proportional function, $\Pi_m = 1/x_{sm}'$, where x_{sm}' is a scaling and translation of x_{sm} by $x_{sm}' = \frac{Kx_{sm}}{(1-M)\lambda} + \frac{1}{\Pi_0}$. The effect of background flow fluctuations (dotted purple line) is relatively weak for stronger shocks. However, its impact increases significantly as the shock becomes very weak. This leads to the strong oscillation in the prediction in the range of $\Pi < 0.2$.

Therefore, the proposed model provides a method to predict the distribution of over-tip shock waves. The overall prediction is reliable, though this model is violated for very weak shock waves near the upstream limit of shock propagation. Three essential factors, the initial state, the mean back ground flow and the flow fluctuations, are identified. The motion of over tip shock waves are governed by a dynamic balance among such factors.

V. FOURIER MODES AND THE LOCK-IN EFFECT OF OVER-TIP SHOCK WAVES

The vortex-shedding and shear-layer flapping motions are primary flow patterns in tip clearance flows that exist under low-subsonic, transonic, and supersonic conditions. When the TLF is

accelerated to the critical state (such as current state: $r_p = 0.297, M_{max} = 1.2, \overline{M}_e = 0.63$), it becomes highly unstable, resulting in the generation and evolution of over-tip shock waves. Fourier analysis and DMD are used to understand the dynamics of over-tip shocks.

The schlieren image captures an integrated measure of the density gradient across the depth of the tip model. In order to perform Fourier or DMD analysis, it is necessary for the shock structures to be uniform along the depth. To achieve this, we assume two-dimensional flows in the clearance and control the spanwise distortions of the shock structures within an acceptable range, ensuring that they are nearly aligned. This is confirmed by examining the static pressure signature at the tip surface along the spanwise direction, and the thickness of observed structures. A case is deemed valid if the discrepancy among five-spanwise pressure taps (as shown in Fig. 4) are less than 1%. The spanwise shock distortions cause the vertical stripes observed in the schlieren images to appear thicker. According to Equ. (20), the thickness of shock waves is approximately the order of 10^{-6} m, which is imaged by a pixel size of about 4×10^{-4} m. Shock spanwise distortion can affect up to two pixels, resulting in shock widths of 1 to 3 pixels. This length scale is much smaller than the average distance between two shocks, which is around 8×10^{-3} m. Therefore, the schlieren image can be considered as an averaged density gradient across the testing section with reduced resolution (a shock represented by one pixel is resolution-reduced to three pixels). Consequently, the Fourier and DMD analysis can be taken as the analysis of uniformly distributed shock structures with slightly-reduced resolution.

Fourier transforms are applied pixel-by-pixel to the measured images. The locations and frequencies of the periodic flow structures are revealed by the resulted Fourier modes. As shown in Fig. 22, three shock oscillation (SO) modes are present on the upper part ($y \geq 115$ mm) of the line $x = -4$ mm. The Strouhal number is defined as $St_c = fc/V_{x,avg}$, with $V_{x,avg} \approx 206.7$ m/s being the averaged x-velocity at the gap exit and $c = 32.8$ mm being the clearance. The strength of the SO rises as the y-coordinate increases. In the lower part of the line $x = -4$ mm, a vortex shedding mode appears when $y \leq 115$ mm. Distinct SO and vortex-shedding modes are visible at $(x, y) = (-4, 115)$ mm. This indicates that shock/shear-layer/vortex-shedding interactions occur in this region. The three observed SO modes are consistent with the first three shear-layer flapping (SLF) modes in Fig. 23, and the vortex-shedding mode coincides the fourth SLF mode. This implies that the SO and vortex-shedding modes are almost locked-in with the SLF modes through these interactions. Side-lobes are observed near the second SO and the second SLF modes. This is due to the interactions of shock waves and shear-layer with the second harmonic

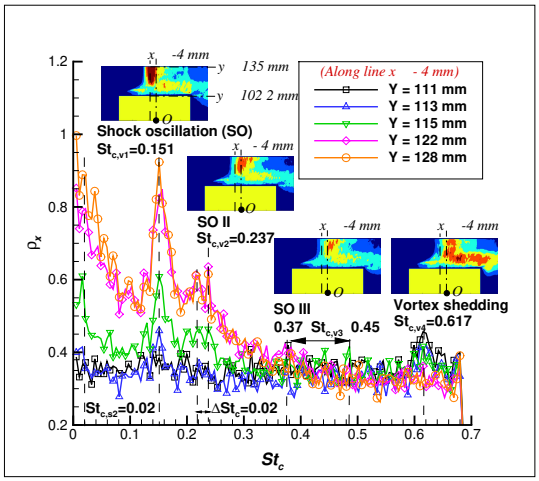

FIG. 22. Spectra and dominant Fourier mode patterns (embedded subfigures) of ρ_x measured by vertical cut-off at five probes along line $x = -4$ mm, which is the location of the strongest shock oscillation. Amplitude is normalized by the maximum peak. Peaks at $St_{c,s1} = 0.01$ and $St_{c,s2} = 0.02$ are system vibrations.

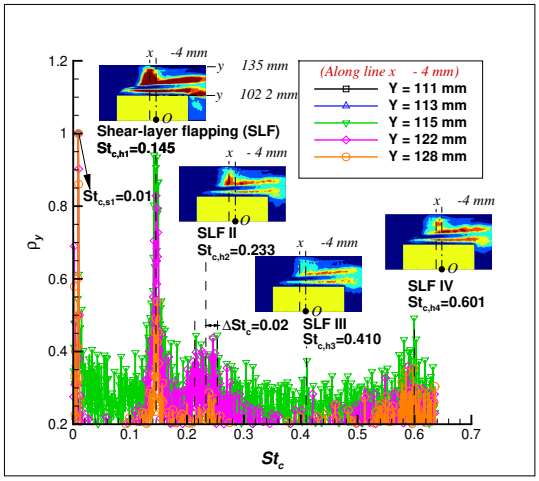

FIG. 23. Spectra and dominant Fourier mode patterns of ρ_y measured by horizontal cutoff at five probes.

of system vibration at $St_{c,s2} = 0.02$, yielding the sub-modes at $St_{c,v2} \pm \Delta St_c$ and $St_{c,h2} \pm \Delta St_c$. Additionally, the coupling effect between the SO and SLF disappears at the third SO mode. This

implies some intermittency exists in the third SO mode, resulting in the unstable frequency of $St_{c,v3} \in [St_{c,h3} - 0.04, St_{c,h3} + 0.04] = [0.37, 0.45]$.

The above-discussed four discrete modes can also be observed under subsonic conditions. They are the SLF modes measured by the horizontal cutoff; however, measured by the vertical cutoff, they are no longer a composition of the SO modes and the vortex shedding mode but pure vortex shedding modes. The change of four modes with the Reynolds number is plotted in Fig. 24. As indicated by the dash-dotted lines, these curves fall into three zones, A, B, and C. Each zone is assigned a sub-figure (Fourier transform of the density gradient) to illustrate corresponding mode pattern. One observes only the SO modes in zone A, in which a vertical shock pattern is observed in the sub-figure. Both the SO and the vortex-shedding modes are observed in zone B, indicating the interaction of these modes. Almost-pure vortex-shedding modes are observed in zone C. Therefore, this zonal feature is determined both by the flow speed and the order of unsteadiness modes. The flow field tends to be dominated by shock waves as flow speed increases, and by vortex shedding as the mode order (frequency) increases. Near-constant patterns (flat lines) are observed for the first and the second modes. This implies that steady coupling of vortex

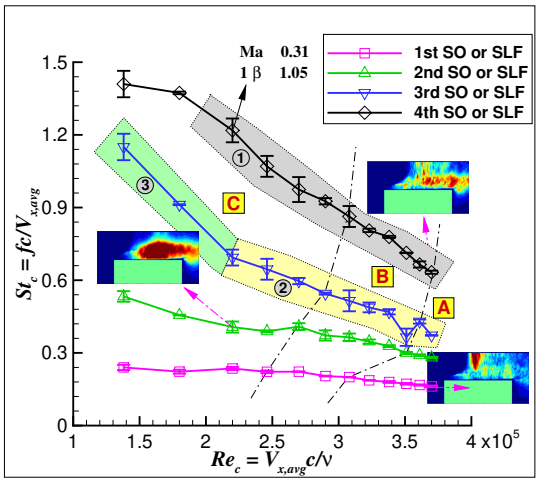

FIG. 24. Change of four Fourier modes with Reynolds number. Squared letters indicate three zones split by dash-dotted lines. Zone A: dominated by shock/compression waves. Zone B: dominated by vortex–shock coupling. Zone C: dominated by vortex shedding. Circled numbers indicate curve segments that carry the same flow mechanism.

shedding and the oscillation of shock/compression waves is established. As indicated by curve segments ② and ③, the flow mechanism of the third mode switches when the pressure ratio increases beyond $r_p = 0.063$ ($\overline{M}_e = 0.31$, $\mathrm{Re_c} = 2.2 \times 10^5$). This switching may be an underlying mechanism of the intermittency feature as observed by the third mode in Fig. 22. Details of this feature are to be discussed by high-fidelity simulations in the near future.

By now, we have achieved that the shock-oscillation frequency is kept the same with the shear-layer flapping. This effect is termed "locked-in by frequency". We are going to prove that, in the meanwhile, shock waves with a given oscillation frequency range is constrained to a specific position range. This effect is termed "locked-in by position". Measured from the Fourier mode patterns, the normalized over-tip shock positions are displayed with respect to the Strouhal number in Fig. 25. Qualitatively identification of three sub-zones, the shock decaying zone, the shock generation zone and the vortex-shock interaction zone, are achieved with the help of two additional operating conditions. As labeled by the squared letters A and B, a clear boundary is observed between the two sub-zones. This implies that not only the frequency, but also the position of the

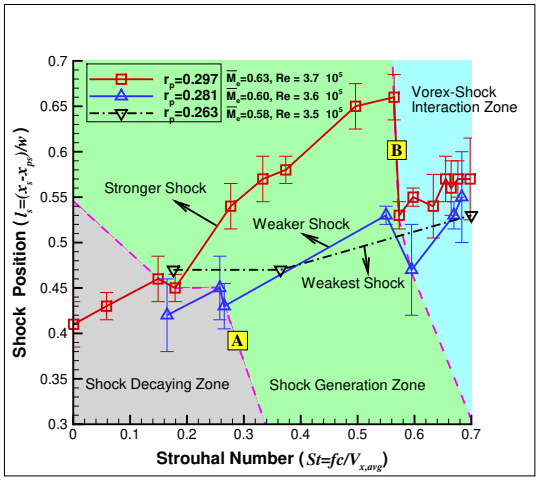

FIG. 25. Shock spatial position changes with oscillation frequency. Positions are measured from Fourier modes, as shown by the subfigures in Fig. 22. x_s, x_{ps}, and w are the x-coordinate of the center fo the SO mode located at position of the maximum mode amplitude, the x-coordinate of the pressure side, and the width of tip clearance, respectively. Color-flooded regions indicate three shock-motion zones (qualitative).

SO mode is locked-in by the SLF mode. Thus, we termed this feature the "lock-in effect", which is essential for blade heat transfer, and is a key factor to be considered in the development of control techniques for TLFs.

This lock-in effect implies that the interaction of vortex-shedding and the over-tip shock waves is governed by some relation between the location and frequency. The frequency synchronizing feature between two related flow structures is easy to understand. The frequency consistency between the SO mode and the SLF mode exists because the vortex motion is a main source for the generation of over-tip shock waves and the shear-layer flapping. The mechanism of the lock-in effect can be explained by the schematic drawing in Fig. 26. Flow structures such as shocks, vortices, separation bubble and the main shear-layer are schematically presented with the schlieren-measured density gradient as the reference background. As one knows, under almost all flow conditions, over-tip vortex shedding happens. Starting from subsonic flow, acoustic waves are generated along with the motion of vortices. As the flow speeds up to transonic, several supersonic cells emerge near the separation bubble and the upper-side of vortices shed from the PS-side. This leads to the generation of shocks that travel upstream. Thus, the frequency of vortex shedding is proportional to the number of shock generation events at a given time scale. If the strength

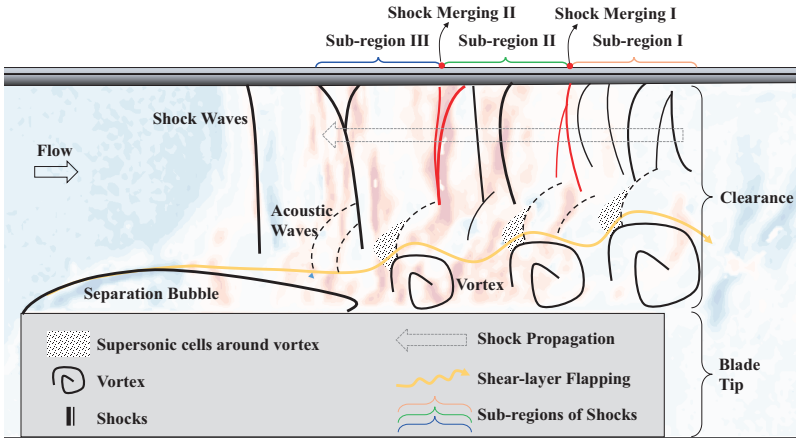

FIG. 26. Schematic view to illustrate the mechanism of the lock-in effect. The schematic flow structures are created based on Fig. 25 and the understanding of TLFs. The schlieren-measured density gradient is set as the background for reference.

of the vortices and background flow is uniformly distributed over time, the so-generated shocks should be uniform. In this case, the shock oscillation frequency should change continuously in the shock region. However, as observed in Fig. 25, the flow field with shocks is partitioned into several sub-regions. The boundary between regions is defined by a frequency jump. The shock oscillation frequency varies in a mild and continuous way until reaching the boundary of two sub-regions when frequency jump occurs. This special feature is schematically illustrated in Fig. 26 by sub-regions. The zonal pattern is explained by the non-uniformity of vortices and the merging of shocks. The non-uniformity of vortex strength and scale leads to the formation of non-uniform shocks. Thus, shock overtaking occurs between the weak-strong shock pairs during the propagation. The boundaries of sub-regions are the locations where shock merging occurs frequently. At the presence of shock merging, the number of shocks decreases and the strength of shocks increases, resulting in more steady shocks (less affected by background flow fluctuations) and lower frequency. At the merging positions, flow speed difference is enlarged by the shock-merging event. This increases the difficulties for downstream shock formation. Consequently, an abrupt observed frequency reduction (wavenumber reduction) occurs at this position.

Following the above discussion, the lock-in effect should widely exist in transonic TLFs at the critical state. To verify this, different blade tip configurations are applied. Together with the flat tip model, as shown in Fig. 27, TLFs over three contoured blade tip models were investigated in the

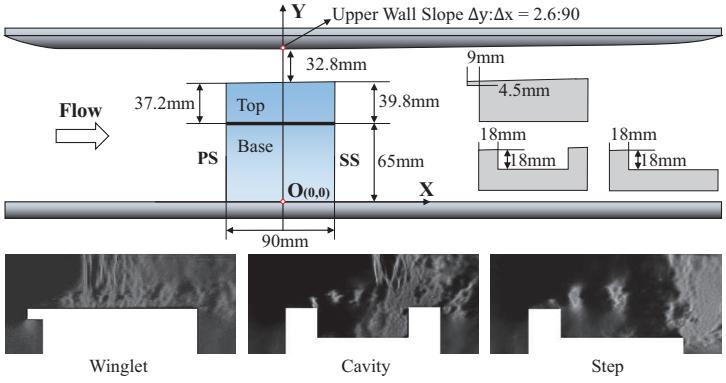

FIG. 27. Blade tip contouring is applied by modifying the top part of the model. The winglet model is designed by extending the tip platform of the flat model. The cavity model is designed as a shallow cavity. The step model is generated by cutting the second squealer of the cavity model.

same wind tunnel under similar operation conditions. The change of blade tip surface termed blade tip contouring (BTC) is a widely used technique to elaborate the TLFs for better performance.

Figure 28 shows the zonal jumping patterns are also observed over the winglet and the cavity model (the step model carries no shocks.). This implies lock-in effects exist for contoured blade tip models. Compared with the flat model, the position of frequency lock-in is similar in the winglet case. For the cavity tip configuration, shock waves are formed much closer to the exit. Position jumping is also observed near $St = 0.2$ and $St = 0.5$. Except for the jumping frequencies, shock positions for other frequencies in contoured blade tips are more stable than the flat model.

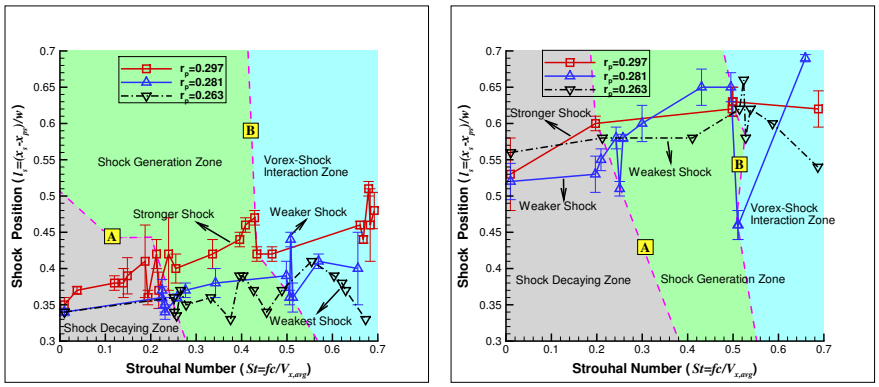

(a) Winglet. (b) Cavity.

FIG. 28. Shock position changes with oscillation frequency over: (a) winglet model; (b) cavity model.

VI. DMD MODES AND THE LIFE CYCLE OF OVER-TIP SHOCK WAVES

The Fourier modes reveal the location and frequency of the dominant flow structures; however, the spatial details are not sufficiently clear. Thus, DMD analysis is performed to obtain more detailed information. In the case of schlieren images, the main idea of the DMD method is as follows. Assume the schlieren images are saved as a set of pixels with dimension $n = p \times q$ in the time series $t = t_0, t_1, \ldots, t_m$. The grayscale image snapshots, $x_t \in \mathbb{R}^{p \times q}$, $t = t_0, t_1, \ldots, t_m$, can be described as a superposition of DMD modes as

$$x_{t_j} = \sum_{i=1}^{r} b_i \phi_i e^{(\delta_i + i\omega_i)(j-1)\Delta t}, \quad j = 1, 2, \ldots, m, \tag{14}$$

where r is the maximum order of the mode after high-order truncation, b_i is the mode amplitude, ϕ_i is the mode eigenvector, δ_i is the mode growth rate (defined as $\delta_i = \text{Real}[\log(\mu_i)]/\Delta t$), ω_i is the mode angular frequency (defined by $\omega_i = \text{Imag}[\log(\mu_i)]/\Delta t$), Δt is the time interval, and μ_i is the eigenvalue of the i-th mode. These image snapshots can be rearranged into two sets, $X = \{x_0, x_1, ..., x_{m-1}\} \in \mathbb{R}^{n\times m}$ and $Y = \{x_1, x_2, ..., x_m\} \in \mathbb{R}^{n\times m}$, which have a constant time interval of $\Delta t = 1/f_s$, where f_s is the sampling rate. Given enough time, the lagged set Y is considered to be a linear mapping of the base set X.[42] Thus, $Y = AX$. The flow field is then decomposed into DMD modes that are described by the eigenvectors and eigenvalues of the matrix A. In this study, the streaming DMD (SDMD) algorithm[43] is applied.

A quasi-linear DMD mapping is achieved with about 2000 snapshots for current study. The mode eigenvector is obtained after applying SDMD. A set of over-determined equations is then constructed from Eq. (14), and the mode amplitude b_i is solved by the least-squares method. Thereafter, the flow field of a single mode is reconstructed by $x_{t_j} = b_i \phi_i e^{(\delta_i + i\omega_i)(j-1)\Delta t}$, $j = 1, 2, ..., m$. For each case, the DMD mode spectrum concerning the first 200 modes is calculated from 16 064 snapshots. For each model, the mode spectra of the vertical and horizontal cutoffs are displayed, and the mode shapes of the dominant modes are given in terms of the mode spectra. The DMD amplitude is defined as the multiple of the norm of the eigenvector and the absolute value of the eigenvalue, $||\phi_i||_2|\mu_i|$. This is normalized by the maximum value to reflect the overall and relative energy of the i-th mode. As a result, the mode amplitude is a measure of the total energy carried by a single mode structure across the distributed area.

As our focus is the transonic operating conditions, we present the critical-state case PD120

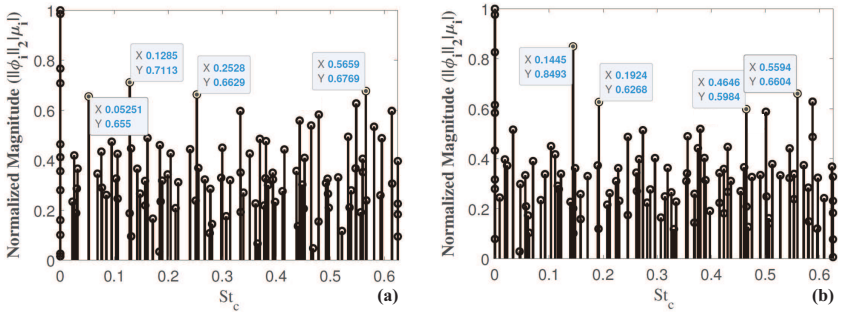

FIG. 29. DMD spectra and the related mode shapes at $r_p = 0.297$ (PD120): (a) VL-cutoff; (b) HD-cutoff.

($r_p = 0.297$, $\overline{M}_e = 0.63$, $\mathrm{Re_c} = 3.7 \times 10^5$). Figure 29 shows the DMD mode spectrum from the VL-cutoff and the HD-cutoff. An overall broadband feature is revealed, which implies that the tip clearance flow under transonic conditions is dominated both by periodic flow structures and turbulent flows. Four relatively dominant modes are labeled under the broadband background. Corresponding DMD mode shapes are displayed in Fig. 30. Based on the location and the mode shape, the first mode in Fig. 30(a) is referred to as an extra SO modes. The second and third modes are consistent with the first two Fourier SO modes shown in Fig. 22. The fourth mode is related to the vortex-shedding mode. The shear-flapping modes are revealed by the labeled peaks in

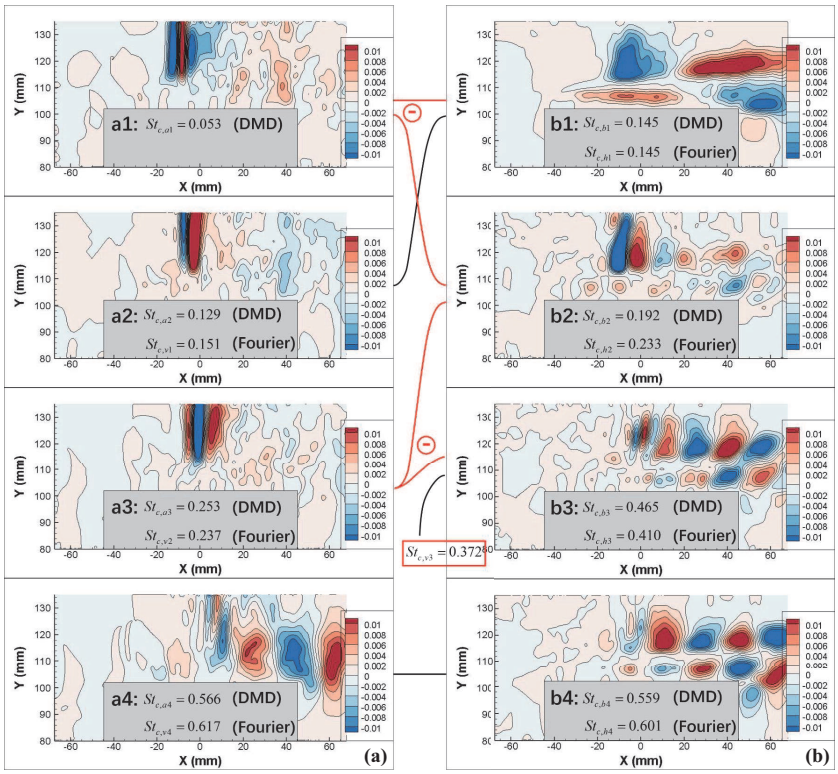

FIG. 30. DMD mode shapes at $r_p = 0.297$ (PD120): (a) VL-cutoff; (b) HD-cutoff. Corresponding Fourier mode frequencies are attached. Coupling effects are illustrated by the linking lines. The symbol ⊖ indicates a subtraction operation. Equivalence is indicated by black linking lines.

Fig. 29(b) with the mode shapes displayed in Figs. 30(b). These modes are consist with the Fourier SLF modes shown in Fig. 23, which are coupled with the vortex-shedding or the SO modes. By examining the Strouhal numbers, the possible coupling relations are $St_{c,a1} \approx St_{c,b2} - St_{c,b1}$, $St_{c,a3} \approx St_{c,b3} - St_{c,b2}$, and $St_{c,a4} \approx St_{c,b4}$.

Due to the zonal features of shock motions, the generation and evolution of over-tip shock waves carries a strong spatially distributing pattern. The life cycle of over-tip shock waves is illustrated in Fig. 31 by the four-phase spatial translation of the DMD modes. First, a dominant vortex-shedding mode is observed downstream of position $x = 5.77$ mm (56.4%w from the PS edge) with $St_c \approx 0.566$. This mode is coupled with the shock generation by vortex/shear-layer/shock interactions. The shock waves are highly unsteady in this region. Thereafter, the shock waves propagate upstream, overtake one another, and merge with weaker shock waves, and the overall oscillation frequency decreases. As shown in Figs. 31(b), the dominant intermediate mode has a frequency of $St_c \approx 0.253$. The intermediate modes should be broadband for shock waves propagation in a free stream. The strong discrete pattern is caused by the interaction with the vortex-shedding and SLF modes, which have almost-constant frequencies. At the final stage, as shown in Fig. 31(d), the shock waves start to fade out and remain spatially still near $x = -10.3$ mm (38.5%w from the PS edge). This yields a low frequency of $St_c \approx 0.053$.

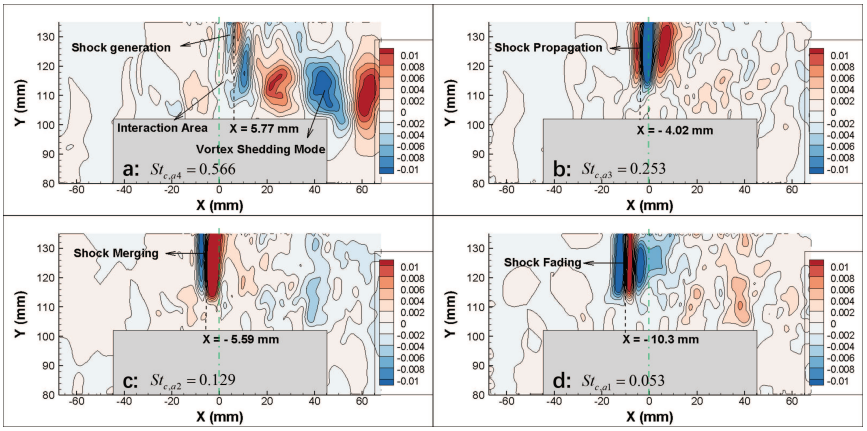

FIG. 31. DMD mode patterns illustrating the process of shock generation and evolution. Four stages are labeled by letters a–d. The position of the shock wave is measured near the first phase-shifting line.

VII. CONCLUSIONS

This paper has described an experimental investigation of common generic blade tip models in a transonic wind tunnel as a means of studying the formation and evolution of the over-tip shock waves in pressure-driven TLFs. The flow fields were measured by pressure taps and time-resolved schlieren visualization. A novel technique, which superposes data from different schlieren cutoffs, was applied to enhance the visualized flow details. The emphasis is on the critical state when the over-tip shock system is highly unsteady. Image processing and additional IDDES simulations are applied to reveal the dynamics of over-tip flow structures. The main conclusions are as follows:

(1) The shock strength satisfies a tooth-like distribution at the critical state. Based on the assumption of sawtooth wave, a simplified model is proposed to predicted the evolution of over-tip shock waves. Good agreements are achieved compared with the measurement. Thus, this model implies that the strength of shock waves during the propagation is determined by the initial shock state, the mean background flow and the flow fluctuations.

(2) Several SO, SLF, and vortex-shedding modes were revealed by Fourier analysis. The SO modes were found to be locked-in with the SLF and vortex-shedding modes. Moreover, spatial analysis implies that both the frequency and position of the SO mode are locked-in by the shear-flapping modes. We termed this feature the "lock-in effect", which also exists in TLFs over contoured blade tips, such as winglet and cavity tips. The mechanism for this effect is explained by the non-uniformity and nonlinear propagation of over-tip shock waves.

(3) DMD analyses were performed to analyze detailed flow structure. Consistency is observed between the DMD modes and the Fourier modes. The spatial information provided by DMD modes reveals that the life cycle of over-tip shock waves is composed of four discrete stages. They are generated in the compression region and propagate upstream. During this process, shock overtaking occurs, resulting in discrete frequency reductions.

ACKNOWLEDGMENTS

This work is supported by grants from the National Key Research and Development Project (Grant No. 2018YFA0703300), the National Natural Science Foundation of China (Grant No. 12102247), the Royal Society (Grant No. IE131709), and the Key Laboratory of Aerodynamic Noise Control of China Aerodynamics Research and Development Center (Grant No. ANCL20210102).

Accepted to Phys. Fluids 10.1063/5.0147216

DATA AVAILABILITY

The data that support the findings of this study are available from the corresponding author upon reasonable request.

APPENDIX: THE APPLIED IDDES MODEL

In order to suppress the Grid Induced Separation (GIS), the Improved Delayed Detached Eddy Simulation (IDDES) model[37,38] is applied under the finite volume framework. This turbulence model enables the large eddy simulation (LES) of boundary layer to achieve scale-resolving simulation (SRS) for high Reynolds number flow. Starting from the $k-\omega$ shear stress transport (SST) background RANS model, a IDDES length scale is applied to the sink term in the k-equation while the ω-equation remains unchanged.[38] Thus, the k- and ω-equations becomes:

$$\begin{aligned}
&\frac{\partial \rho k}{\partial t}+\nabla\cdot(\rho \mathbf{U}k)=\nabla\cdot[(\mu+\sigma_k\mu_t)\nabla k]+P_k-\rho\sqrt{k^3}/l_{IDDES},\\
&\frac{\partial \rho \omega}{\partial t}+\nabla\cdot(\rho \mathbf{U}\omega)=\nabla\cdot[(\mu+\sigma_\omega\mu_t)\nabla \omega]+P_k+2(1-F_1)\rho\sigma_{\omega_2}\frac{\nabla k\cdot\nabla\omega}{\omega}+\alpha\frac{\rho}{\mu_t}P_k-\beta\rho\omega^2,
\end{aligned} \tag{15}$$

in which, $\mu_t=\rho\frac{a_1\cdot k}{max(a_1\cdot\omega,F_2\cdot S)}$, $a_1=0.31$, F_1 and F_2 denote the SST blending functions.[44] Coefficients $\sigma_k,\sigma_\omega,\alpha,\beta$ are then achieved from the blending function $g=g_1\cdot F_1+g_2\cdot(1-F_1)$ by replacing the marker g to be $\sigma_k,\sigma_\omega,\alpha$ or β. Coefficients in the boundary ($\bullet_1$, from Wilcox's model[45]) and in the free stream ($\bullet_2$, from the standard $k-\varepsilon$ model[46]) are used with values list as:

$$\begin{aligned}
&\alpha_1=5/9,\quad \alpha_2=0.44,\ \beta_1=0.075,\ \beta_2=0.0828,\\
&\sigma_{k1}=0.85,\ \sigma_{k2}=1.0,\ \sigma_{\omega_1}=0.5,\quad \sigma_{\omega_2}=0.856.
\end{aligned}$$

A simplified version of IDDES length scale is applied, which is blended from the RANS and LES length scale as

$$l_{IDDES}=\tilde{f}_d\cdot l_{RANS}+(1-\tilde{f}_d)\cdot l_{LES}, \tag{16}$$

where

$$l_{LES} = C_{DES}\Delta,\ l_{RANS} = \frac{\sqrt{k}}{C_\mu \omega},$$
$$C_{DES} = C_{DES1}\cdot F_1 + C_{DES2}\cdot(1-F_1),$$
$$\Delta = min\{C_\omega max[d_\omega, h_{max}], h_{max}\},$$
$$\tilde{f}_d = max\{1-f_{dt}, f_b\}.$$
$$f_{dt} = 1 - tanh[(C_{dt1}r_{dt})^{C_{dt2}}],$$
$$f_b = min\{2e^{-9\cdot(0.25-d_w/h_{max})^2}, 1.0\}.$$

in which, d_w is the distance to the nearest wall, h_{max} is the maximum edge length of the grid element and the empirical coefficients are set as:

$$C_{DES1} = 0.78,\ C_{DES2} = 0.61,\ C_\omega = 0.15,\ C_{dt1} = 20,\ C_{dt2} = 3.$$

APPENDIX: RELATIONSHIP BETWEEN THE SHOCK STRENGTH AND DENSITY GRADIENT

The density ratio across the shock can be derived from the Rankine-Hugoniot relation to be

$$\frac{\rho_2}{\rho_1} = \frac{(\gamma+1)(p_2/p_1)+(\gamma-1)}{(\gamma+1)+(\gamma-1)(p_2/p_1)}. \tag{17}$$

Following the definition of shock strength, $\Pi = (p_2-p_1)/p_1 = p_2/p_1 - 1$, the strength of shock is obtained as

$$\Pi = \frac{2\gamma(1-\rho_2/\rho_1)}{-(\gamma+1)+(\gamma-1)(\rho_2/\rho_1)}. \tag{18}$$

The density gradient ρ_x across the shock can be estimated by

$$\rho_x = (\rho_2-\rho_1)/\delta, \tag{19}$$

where δ is the thickness of shocks. As proposed by Puckett et al.,[47] the thickness of shock can be estimated by

$$\delta = \frac{8\nu\gamma}{2(\gamma+1)a_0}\frac{u_s/a_0+1}{u_s/a_0-1}, \tag{20}$$

where ν is the coefficient of viscosity, a_0 is the background sound velocity, u_s is the moving speed of a normal shock, which is related to the shock strength by

$$u_s/a_0 = \sqrt{1+\frac{\gamma+1}{2\gamma}\Pi}. \tag{21}$$

Combine Equs. 18-21, one can find a cubic equation with one unknown, u_s/a_0. This cubic equation has two negative solutions (non-physical) and one positive that is expressed as

$$u_s/a0 = \frac{-\rho_1 - \sqrt{m^2 + mn - n\rho_1}}{m - \rho_1}, \tag{22}$$

where ρ_1 is the density immediately before the shock; m, n are linear functions of density gradient expressed as

$$m = \frac{2\gamma(\gamma-1)\nu}{(\gamma+1)a_0}\rho_x,\ n = -\frac{2\gamma\nu}{a_0}\rho_x. \tag{23}$$

Thus, the shock strength is related to density gradient by

$$\Pi = \frac{2\gamma}{\gamma+1}\left(\frac{-\rho_1 - \sqrt{m^2 + mn - n\rho_1}}{m - \rho_1}\right)^2 - \frac{2\gamma}{\gamma+1}. \tag{24}$$

REFERENCES

[1]J. D. Denton, "The 1993 IGTI scholar lecture - loss mechanisms in turbomachines," Journal of Turbomachinery **115**, 621–656 (1993).

[2]Y. Wang, W. Zhang, D. Huang, S. Jiang, Y. Chen, and G. Ma, "Control strategies for tip leakage vortex using inclined squealer rim in axial turbines," Physics of Fluids **34**, 036101 (2022).

[3]A. P. Wheeler and R. D. Sandberg, "Numerical investigation of the flow over a model transonic turbine blade tip," Journal of Fluid Mechanics **803**, 119–143 (2016).

[4]M. Hewkin-Smith, G. Pullan, S. D. Grimshaw, E. M. Greitzer, and Z. S. Spakovszky, "The role of tip leakage flow in spike-type rotating stall inception," in: *ASME Turbo Expo 2017: Turbomachinery Technical Conference and Exposition*, Vol. 2D: Turbomachinery (2017) p. V02DT46A009.

[5]L. Li, Z. Wang, X. Li, and Z. Zhu, "Multiscale modeling of tip-leakage cavitating flows by a combined volume of fluid and discrete bubble model," Physics of Fluids **33**, 062104 (2021).

[6]J. P. Bindon, "The measurement and formation of tip clearance loss," Journal of Turbomachinery **111**, 257–263 (1989).

[7]A. P. S. Wheeler, N. R. Atkins, and L. He, "Turbine blade tip heat transfer in low speed and high speed flows," Journal of Turbomachinery **133**, 041025 (2011).

[8]W. Shang, D. Li, K. Luo, J. Fan, and J. Liu, "Effects of tip clearance size on vortical structures and turbulence statistics in tip-leakage flows: A direct numerical simulation study," Physics of Fluids **33**, 085127 (2021).

[9]X. He, Z. Fang, G. Rigas, and M. Vahdati, "Spectral proper orthogonal decomposition of compressor tip leakage flow," Physics of Fluids **33**, 105105 (2021).

[10]J. Hou, Y. Liu, L. Zhong, W. Zhong, and Y. Tang, "Effect of vorticity transport on flow structure in the tip region of axial compressors," Physics of Fluids **34**, 055102 (2022).

[11]S. Babu, P. Chatterjee, and A. M. Pradeep, "Transient nature of secondary vortices in an axial compressor stage with a tandem rotor," Physics of Fluids **34**, 065125 (2022).

[12]W. Feng, X. Zhao, C. Wang, Q. Wang, and Y. Zhou, "Experimental study on the rapid establishment of the transonic gap flow field," Physics of Fluids **33**, 016101 (2021).

[13]M. Abdelmwgoud and A. Mohany, "Control of the self-sustained shear layer oscillations over rectangular cavities using high-frequency vortex generators," Physics of Fluids **33**, 045115 (2021).

[14]Navrose and S. Mittal, "Lock-in in vortex-induced vibration," Journal of Fluid Mechanics **794**, 565–594 (2016).

[15]S. W. Lee and S. U. Kim, "Tip gap height effects on the aerodynamic performance of a cavity squealer tip in a turbine cascade in comparison with plane tip results: part 1—tip gap flow structure," Experiments in Fluids **49**, 1039–1051 (2010).

[16]S. E. Lee and S. W. Lee, "Over-tip leakage flow and loss in a turbine cascade equipped with suction-side partial squealers," International Journal of Heat and Fluid Flow **61**, 575–584 (2016).

[17]Z. Saleh, E. J. Avital, and T. Korakianitis, "Effect of in-service burnout on the transonic tip leakage flows over flat tip model," Proceedings of the Institution of Mechanical Engineers, Part A: Journal of Power and Energy **234**, 655–669 (20

[18]R. Mailach, I. Lehmann, and K. Vogeler, "Periodical unsteady flow within a rotor blade row of an axial compressor - Part II: Wake-tip clearance vortex interaction," Journal of Turbomachinery **130**, 041005 (2008).

[19]B. Deveaux, C. Fournis, V. Brion, J. Marty, and A. Dazin, "Experimental analysis and modeling of the losses in the tip leakage flow of an isolated, non-rotating blade setup," Experiments in Fluids **61**, 126 (2020).

[20]M. C. Jacob, E. Jondeau, B. Li, and J. C. Boudet, "Tip leakage flow: Advanced measurements and analysis," in: *28th AIAA/CEAS Aeroacoustics Conference* (2016) p. 2016-2823.

[21]A. Fischer, J. Knig, J. Czarske, C. Rakenius, G. Schmid, and H.-P. Schiffer, "Investigation of the tip leakage flow at turbine rotor blades with squealer cavity,"

Experiments in Fluids **54**, 1462 (2013).

[22]H. Shi, T. Wang, M. Zhao, and Q. Zhang, "Modal analysis of non-ducted and ducted propeller wake under axis flow," Physics of Fluids **34**, 055128 (2022).

[23]S. K. Karthick, "Shock and shear layer interactions in a confined supersonic cavity flow," Physics of Fluids **33**, 066102 (2021).

[24]S. M. V. Rao and S. K. Karthick, "Studies on the effect of imaging parameters on dynamic mode decomposition of time-resolved schlieren flow images," Aerospace Science and Technology **88**, 136–146 (2019).

[25]H. E. Gallus, "ERCOFTAC test case 6 axial flow turbine stage," in: *Seminar and Workshop on 3D Turbomachinery flow prediction III* (1995).

[26]I. Nikolos, D. Douvikas, and K. Papailiou, "Theoretical modelling of relative wall motion effects in tip leakage flow," in: *ASME 1995* International Gas Turbine and Aeroengine Congress and Exposition (1995) p. 95-GT-088.

[27]J. Fang, Y. Gao, Y. Liu, L. Lu, Y. Yao, and C. L. Ribault, "Direct numerical simulation of a tip-leakage flow in a planar duct with a longitudinal slit," Physics of Fluids **31**, 125108 (2019).

[28]K. L. Suder and M. L. Celestina, "Experimental and computational investigation of the tip clearance flow in a transonic axial compressor rotor," Journal of Turbomachinery **118**, 218–229 (1996).

[29]C.-M. Jang, M. Furukawa, and M. Inoue, "Analysis of vortical flow field in a propeller fan by LDV measurements and LES—Part I: Three-dimensional vortical flow structures," Journal of Fluids Engineering **123**, 748–754 (2001).

[30]G. S. Azad, J.-C. Han, S. Teng, and R. J. Boyle, "Heat transfer and pressure distributions on a gas turbine blade tip," in: *ASME Turbo Expo 2000: Power for Land, Sea, and Air* (2000) p. V003T01A002.

[31]C. Bringhenti and J. R. Barbosa, "Effects of turbine tip clearance on gas turbine performance," in: *ASME Turbo Expo 2008: Power for Land, Sea, and Air*, Vol. 6: Turbomachinery, Parts A, B, and C (2008) pp. 1715–1721.

[32]J. Moore and K. M. Elward, "Shock formation in overexpanded tip leakage flow," in: *International Gas Turbine and Aerongine Congress and Exposition* (1992) p. V001T01A001.

[33]A. Z. Shahneh and F. Motallebi, "Effect of submerged vortex generators on shock-induced separation in supersonic flow," Journal of Aircraft **46**, 856–863 (2009).

[34]Wikipedia, "Gamma correction," (2022).

[35]T. J. Whalen and S. J. Laurence, "Experiments on the separation of sphere clusters in hypersonic flow," Experiments in Fluids **62**, 70 (2021).

[36]G. Settles, *Schlieren and Shadowgraph Techniques: Visualizing Phenomena in Transparent Media* (Springer, Berlin, Germany, 2001) p. 394.

[37]M. L. Shur, P. R. Spalart, M. K. Strelets, and A. K. Travin, "A hybrid RANS-LES approach with delayed-DES and wall-modelled LES capabilities," International Journal of Heat and Fluid Flow **29**, 1638–1649 (2008).

[38]M. S. Gritskevich, A. V. Garbaruk, J. Schütze, and F. R. Menter, "Development of DDES and IDDES formulations for the k-ω shear stress transport model," Flow, Turbulence and Combustion **88**, 431–449 (2012).

[39]J. Yan, X. Yang, Z. Niu, X. Tang, J. Ding and P. Weng, "A robust implicit computational framework for compressible flow simulations using high order Discontinuous Galerkin method," Chinese Journal of Aeronautics (2023, Accepted).

[40]X. Yang, J. Cheng, H. Luo, and Q. Zhao, "Robust implicit direct discontinuous Galerkin method for simulating the compressible turbulent flows," AIAA Journal **57**(3), 1113-1132 (2018).

[41]I. Rudnick, "On the attenuation of a repeated sawtooth shock wave," The Journal of the Acoustical Society of America **25**, 1012–1013 (1953).

[42]P. J. Schmid, "Dynamic mode decomposition of numerical and experimental data," Journal of Fluid Mechanics **656**, 5–28 (2010).

[43]M. S. Hemati, M. O. Williams, and C. W. Rowley, "Dynamic mode decomposition for large and streaming datasets," Physics of Fluids **26**, 111701 (2014).

[44]F. R. Menter, "Two-equation eddy-viscosity turbulence models for engineering applications," AIAA Journal **32**(8), 1598–1605 (1994).

[45]D. C. Wilcox, "Reassessment of the scale-determining equation for advanced turbulence models," AIAA Journal **26**(11), 1299–1310 (1988).

[46]B. E. Launder and B. I. Sharma, "Application of the energy-dissipation model of turbulence to the calculation of flow near a spinning disc," Letters in Heat and Mass Transfer **1**, 131–137 (1974).

[47]A. E. Puckett and H. J. Stewart, "The thickness of a shock wave in air," Quarterly of Applied Mathematics **7**, 457–463 (1950).

Accepted to Phys. Fluids 10.1063/5.0147216

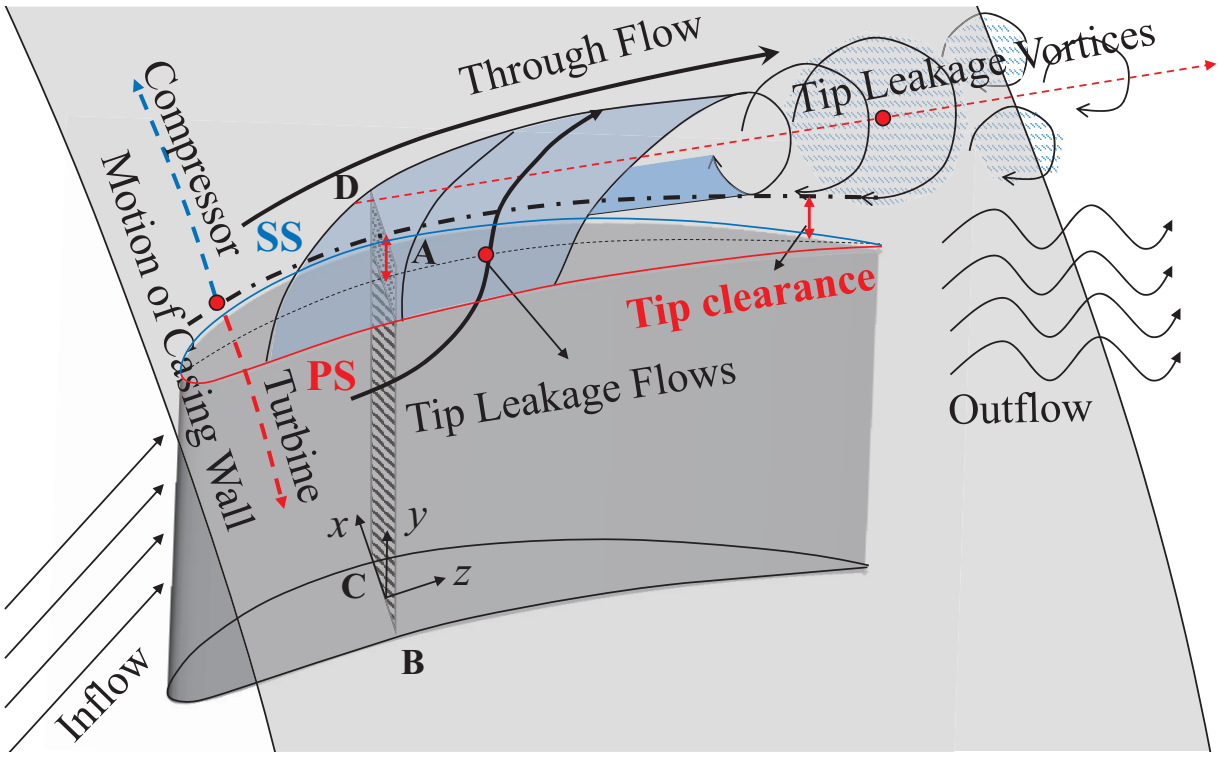

Accepted to Phys. Fluids 10.1063/5.0147216

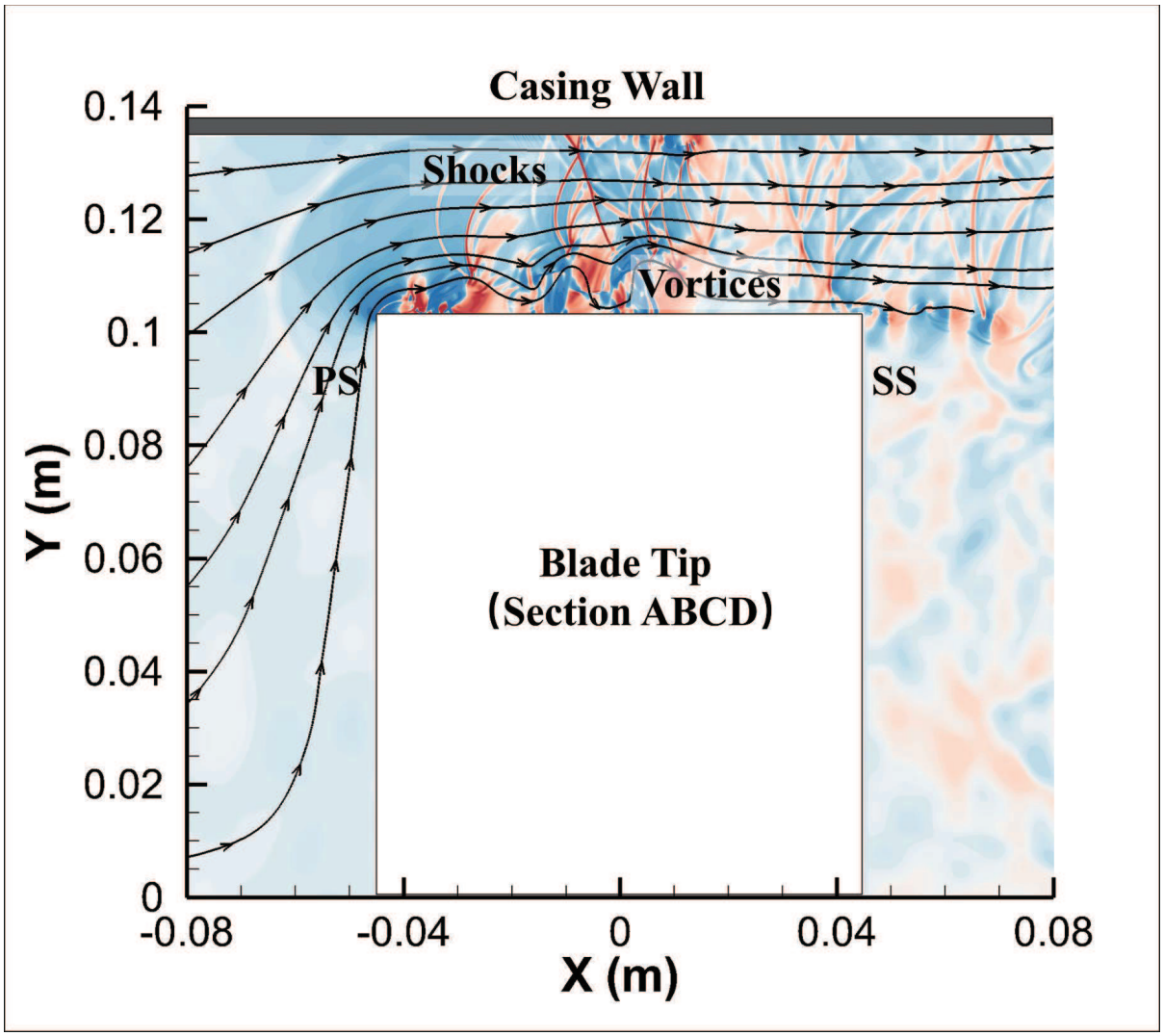

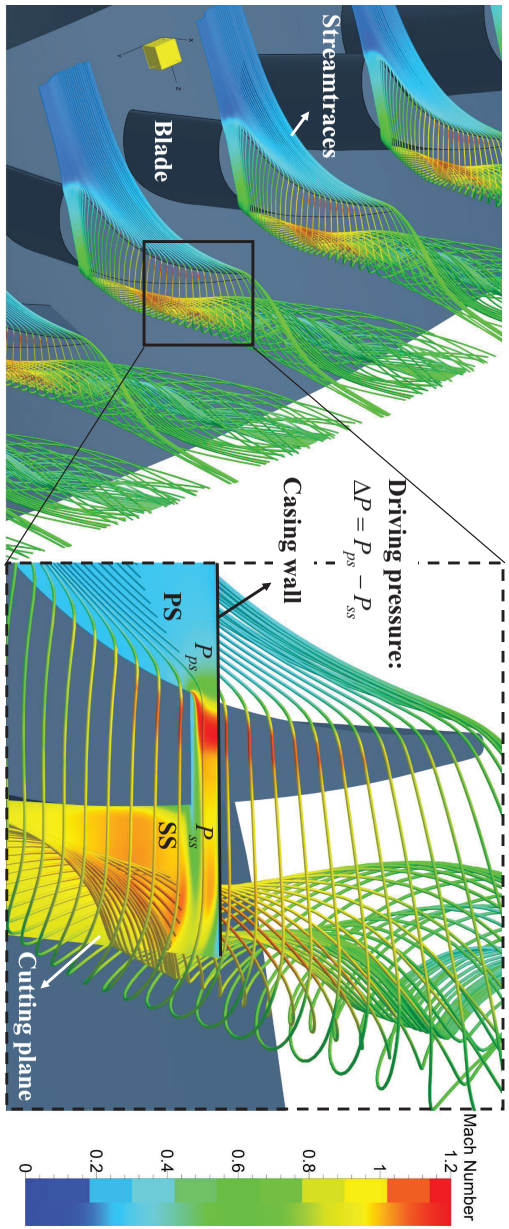

Accepted to Phys. Fluids 10.1063/5.0147216

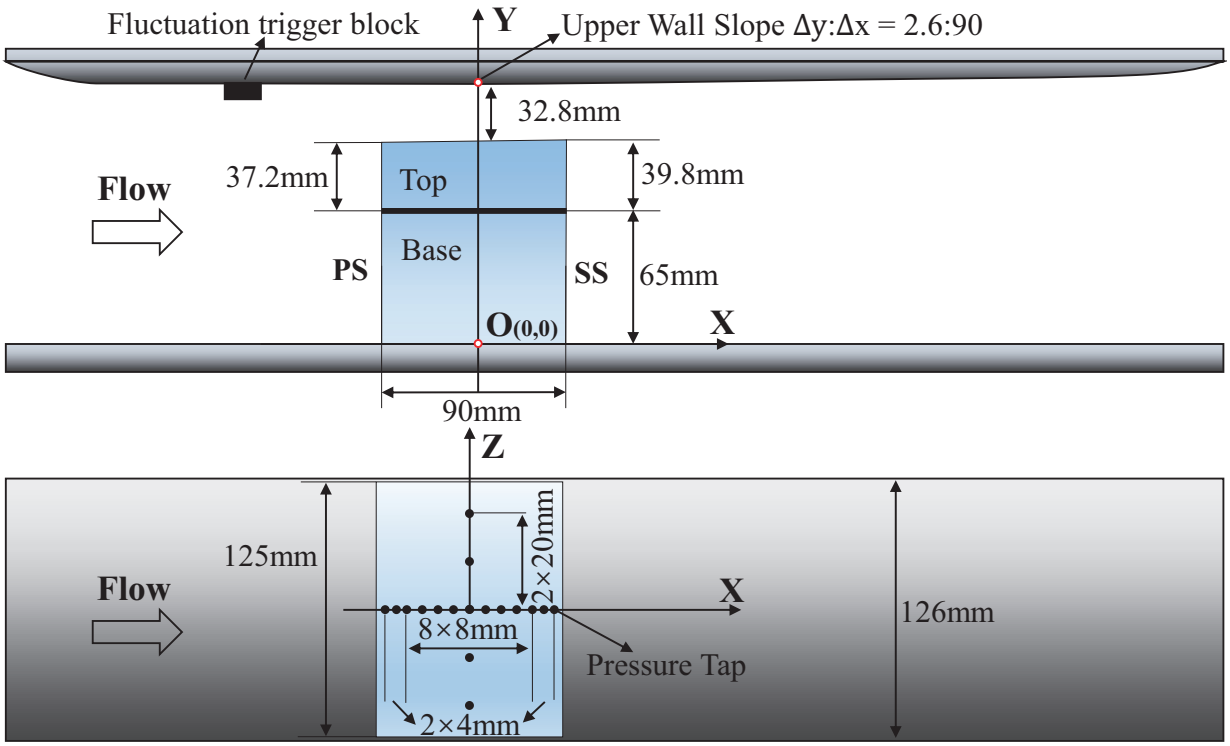

Accepted to Phys. Fluids 10.1063/5.0147216

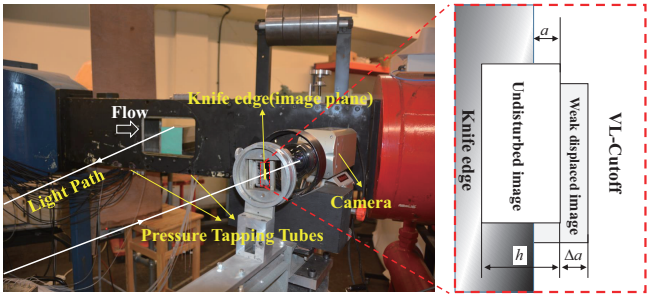

(a) Photo of the wind tunnel.

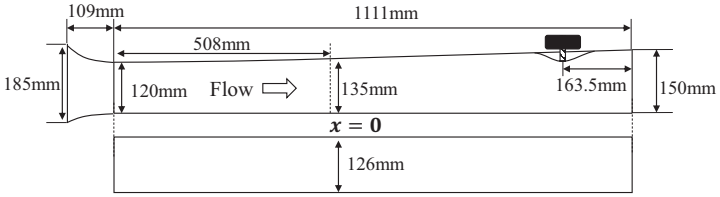

(b) Profile of the wind tunnel.

Accepted to Phys. Fluids 10.1063/5.0147216

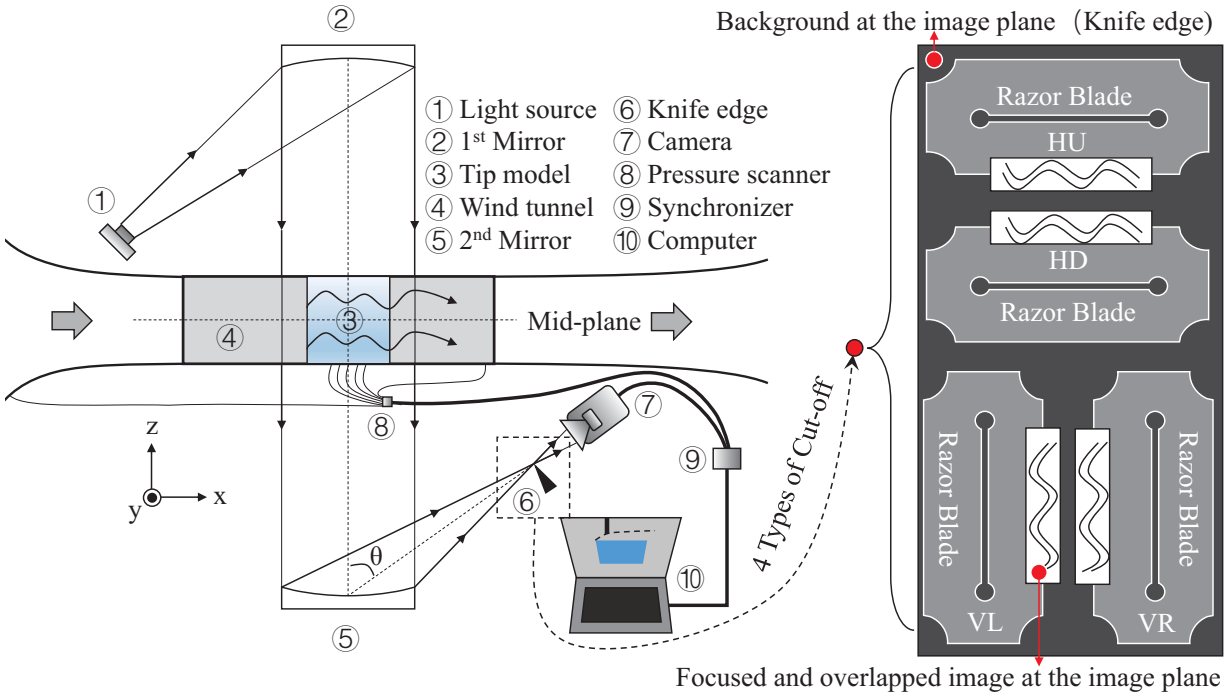

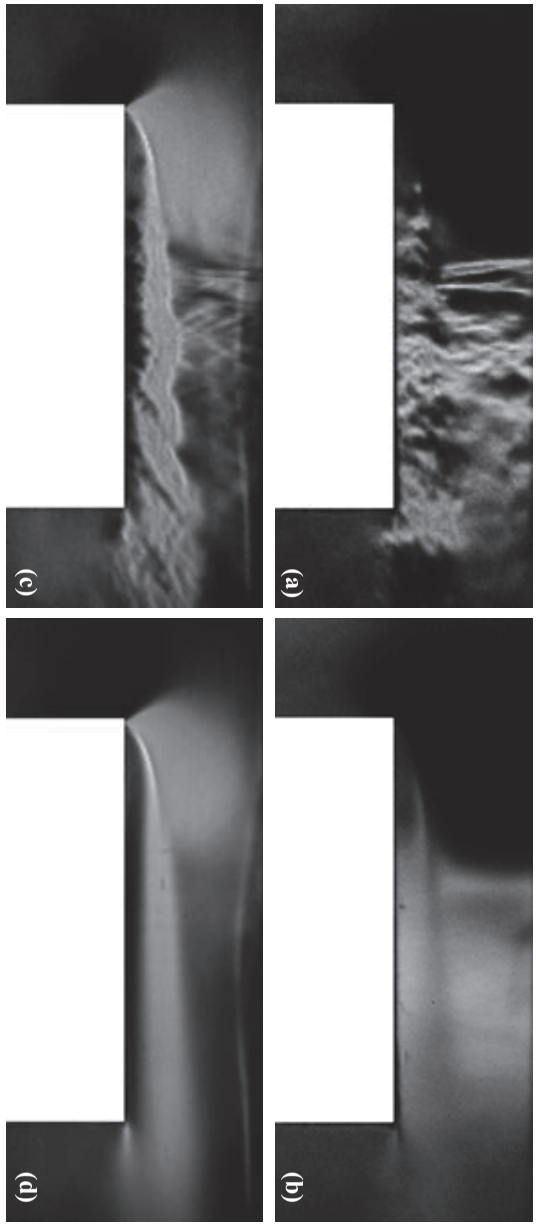

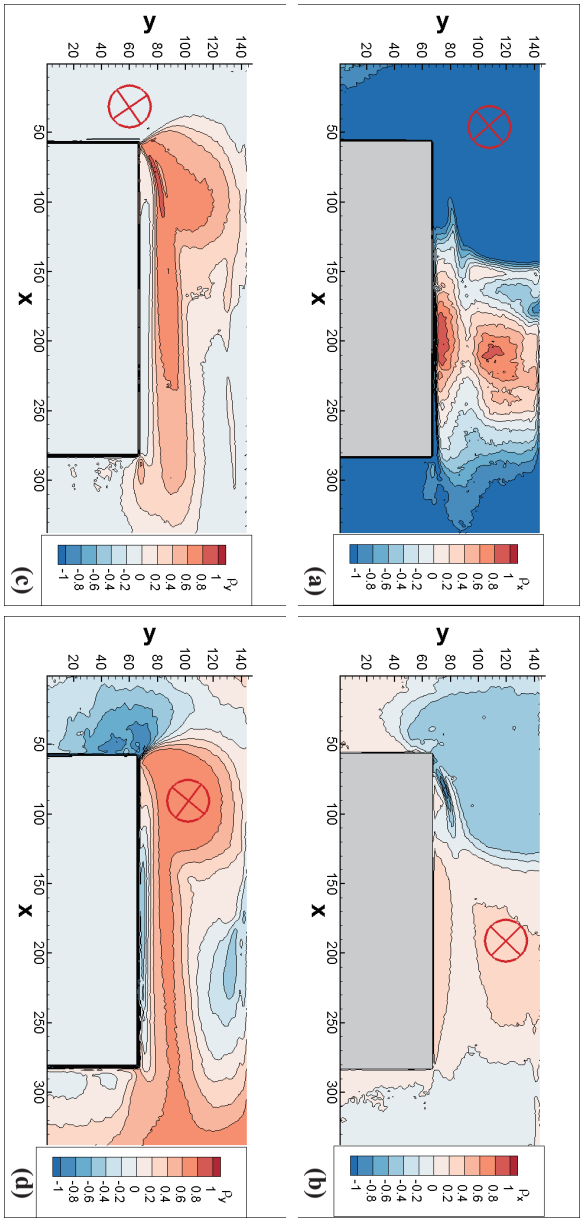

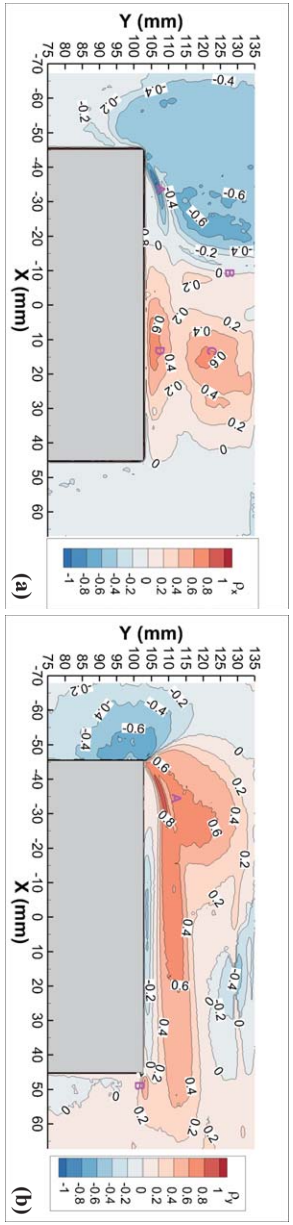

Accepted to Phys. Fluids 10.1063/5.0147216

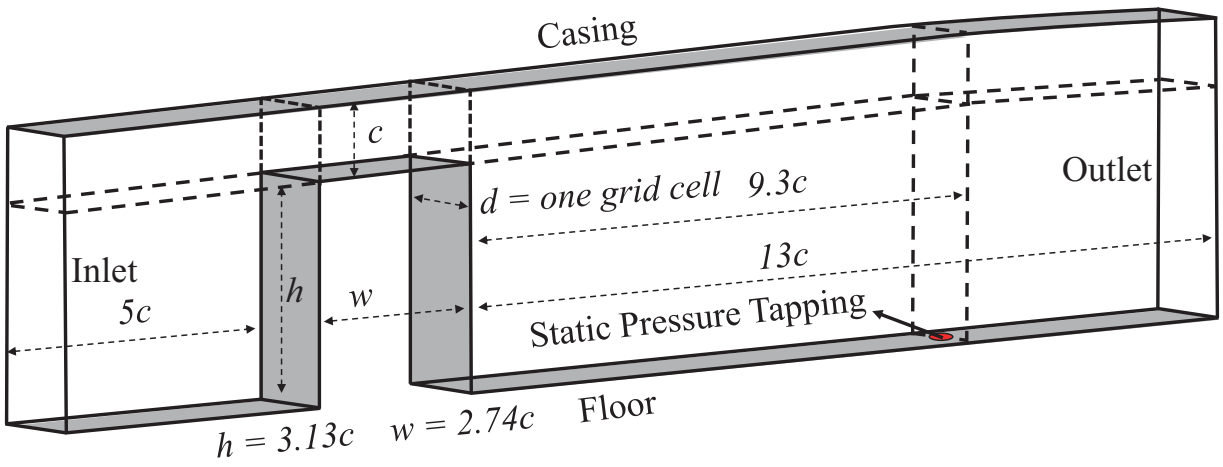

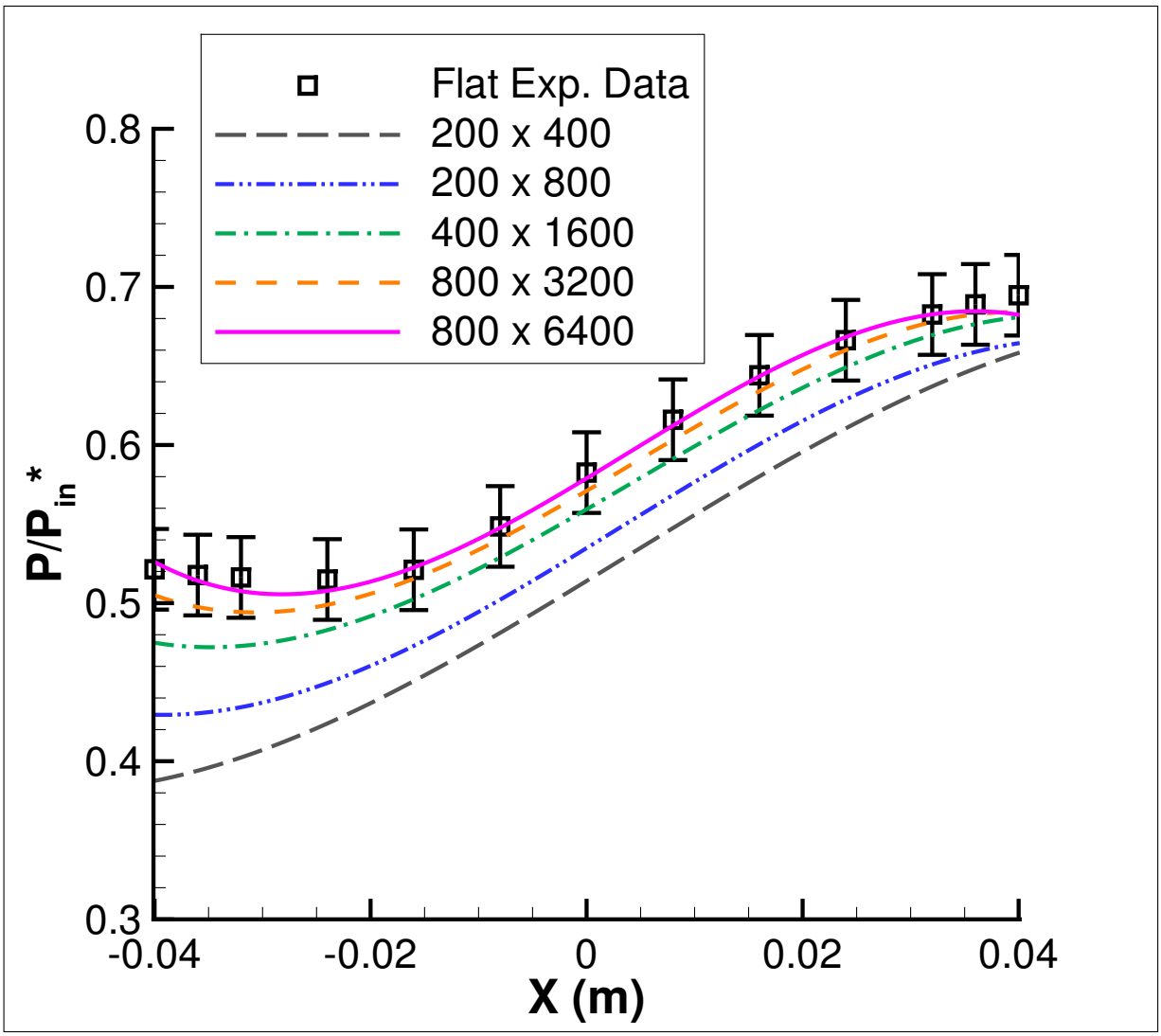

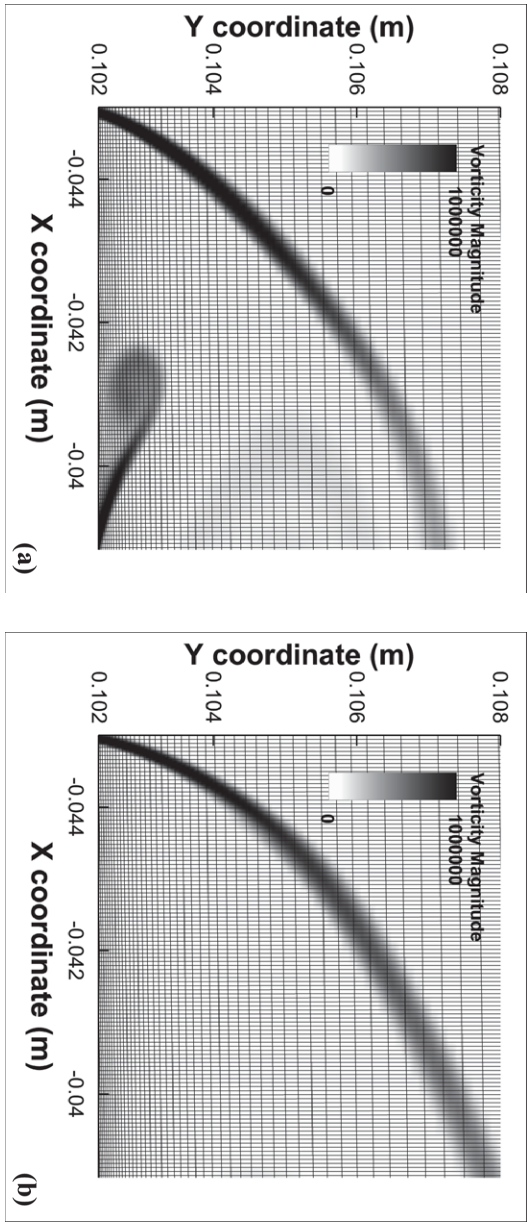

Accepted to Phys. Fluids 10.1063/5.0147216

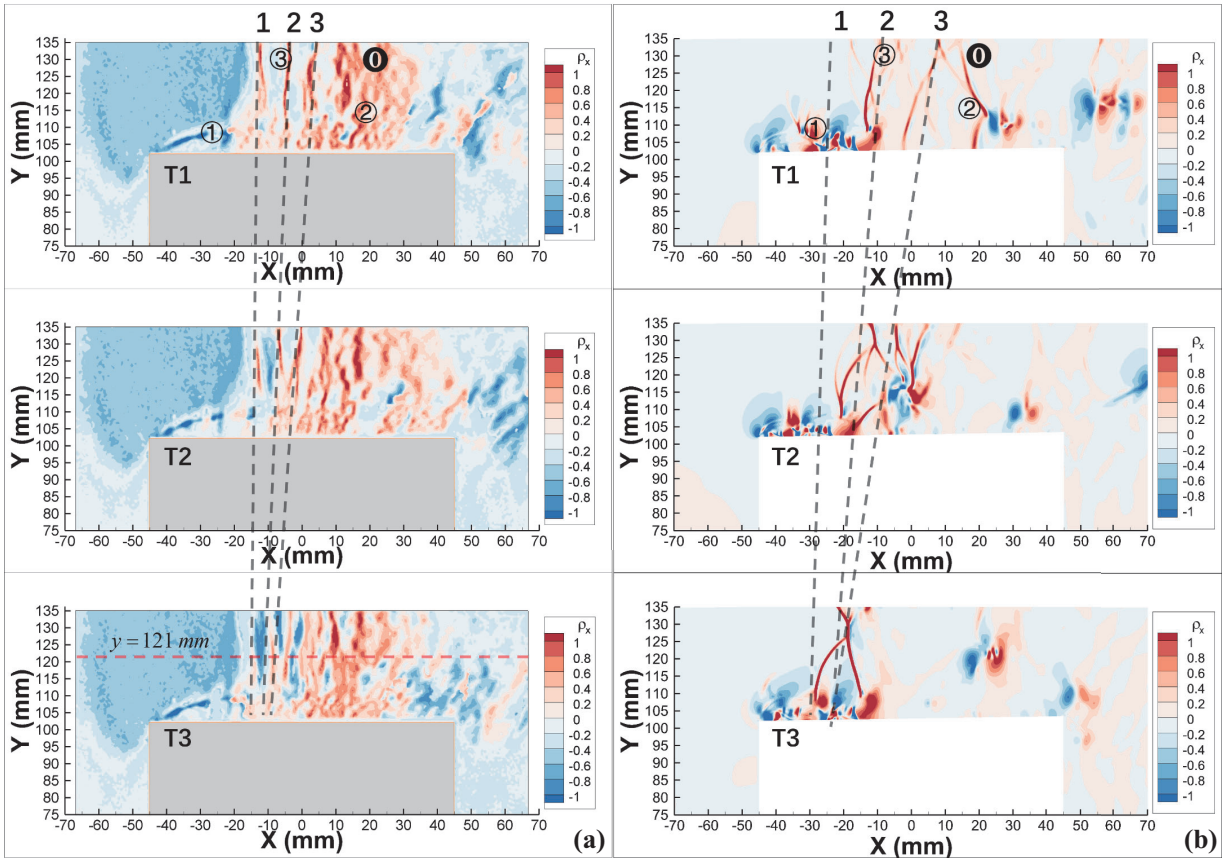

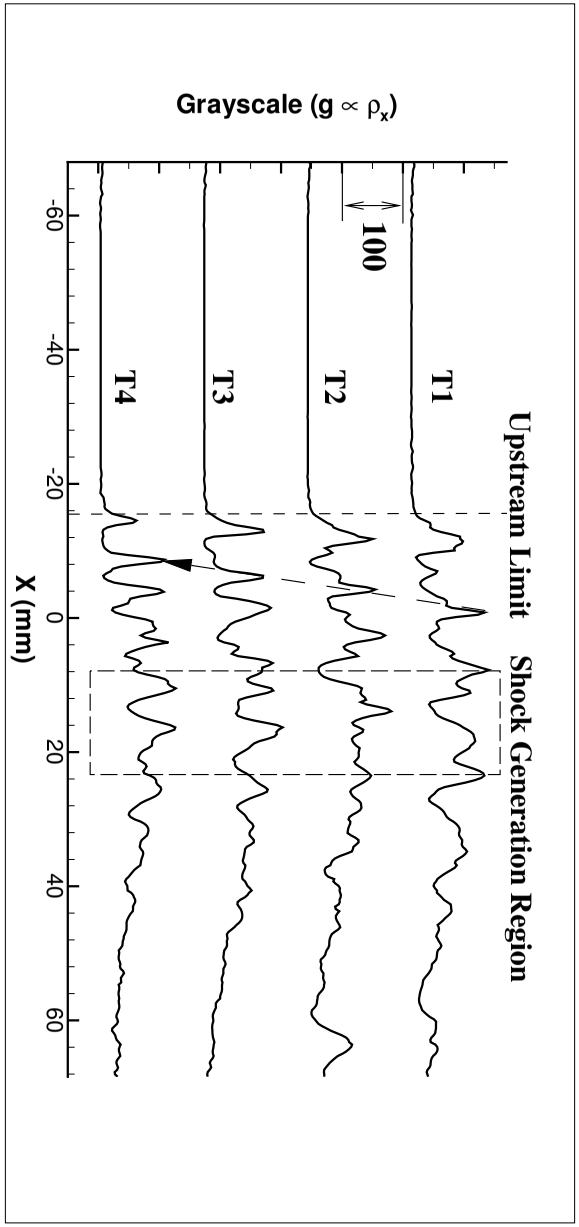

Accepted to Phys. Fluids 10.1063/5.0147216

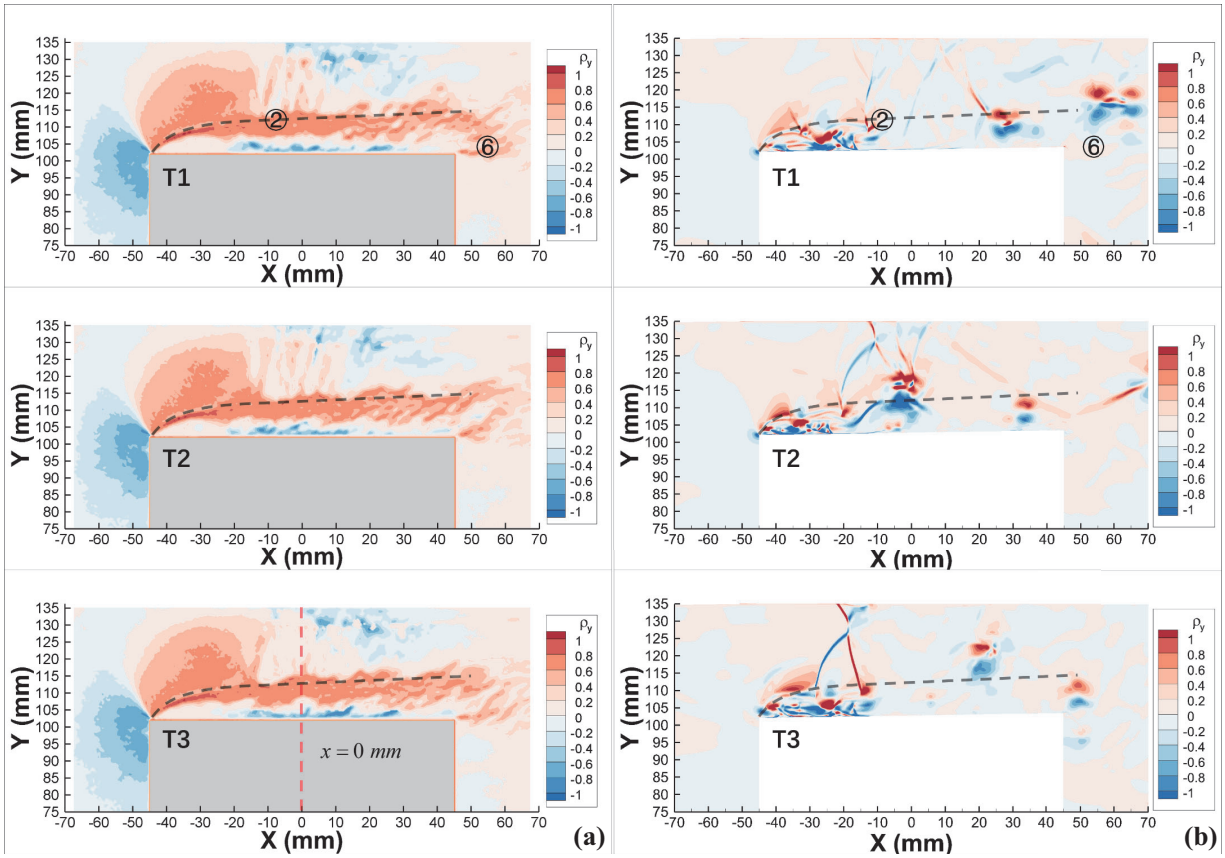

Physics of Fluids

PLEASE CITE THIS ARTICLE AS DOI: 10.1063/5.0147216

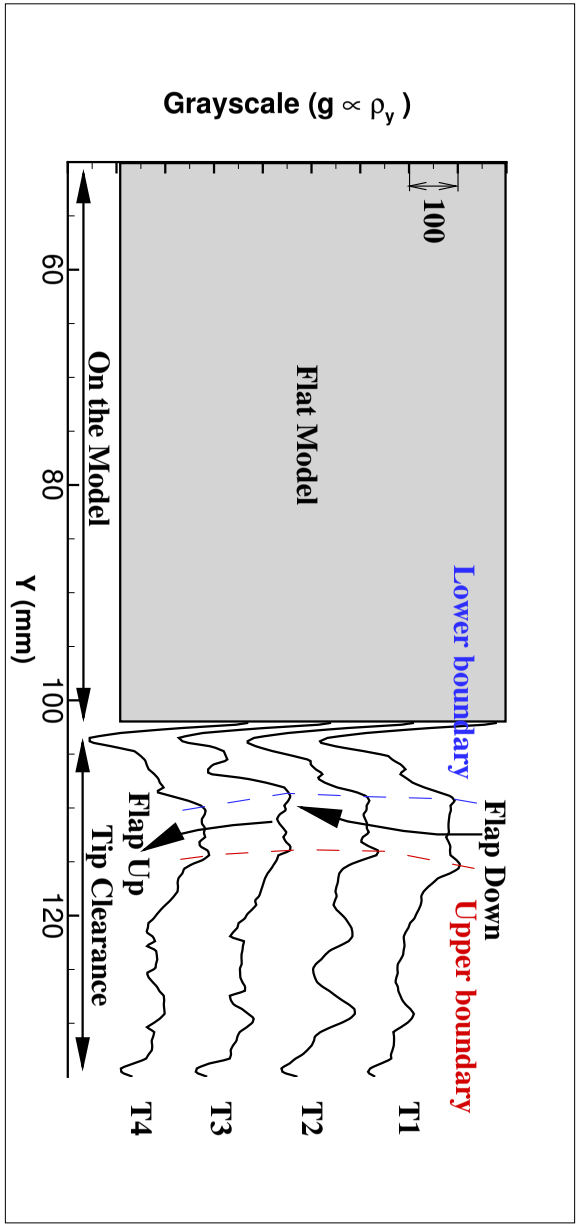

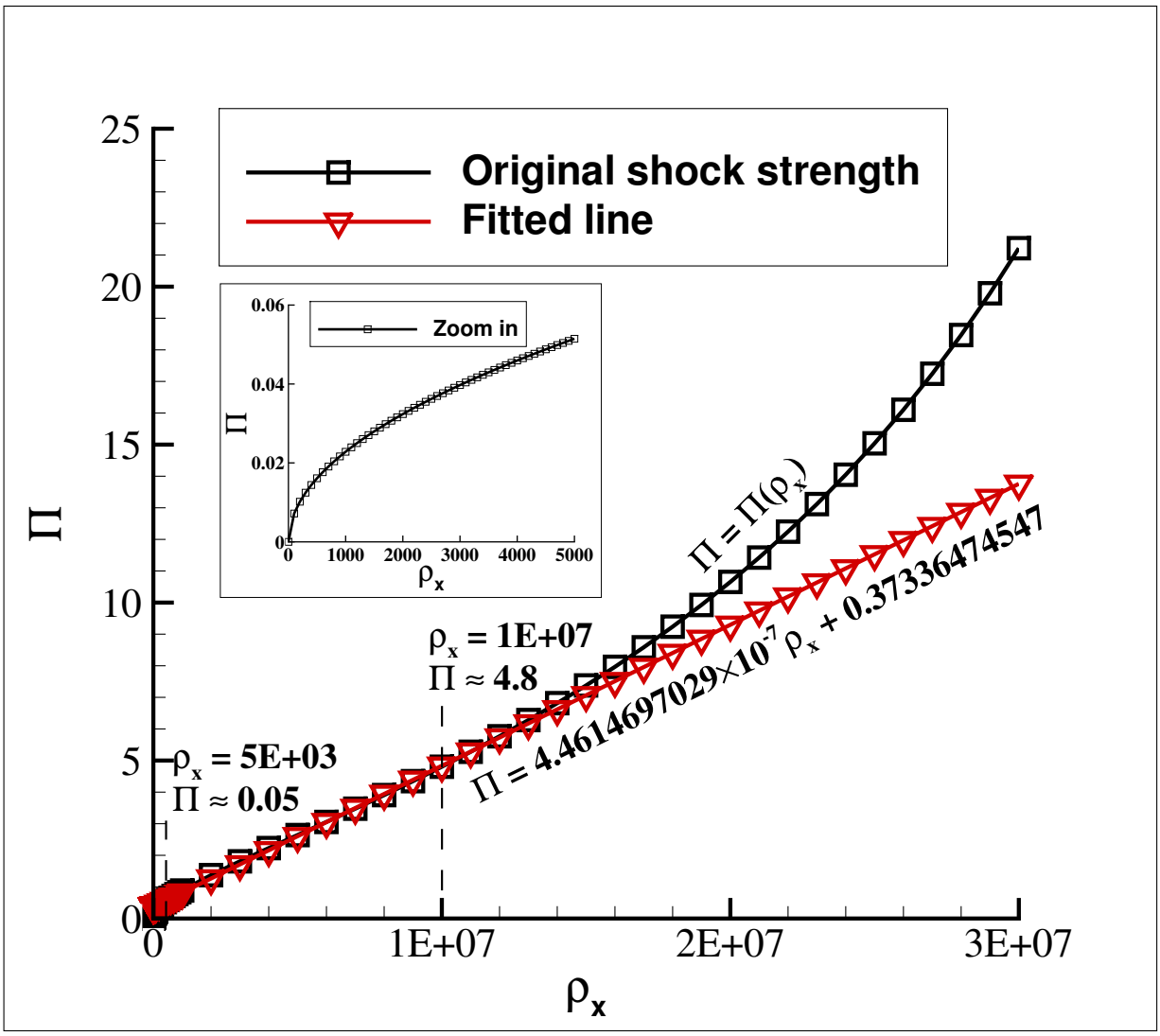

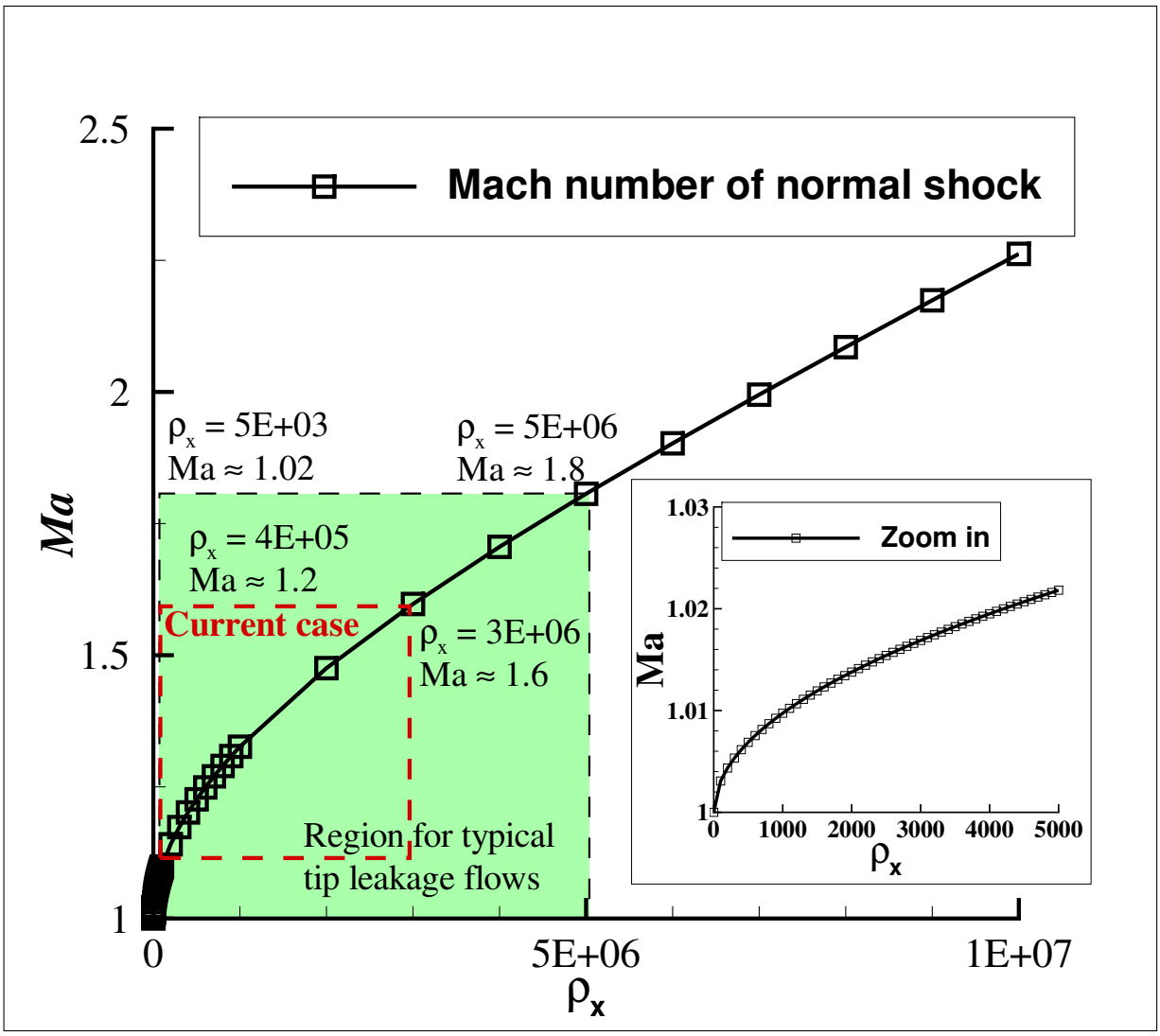

Accepted to Phys. Fluids 10.1063/5.0147216

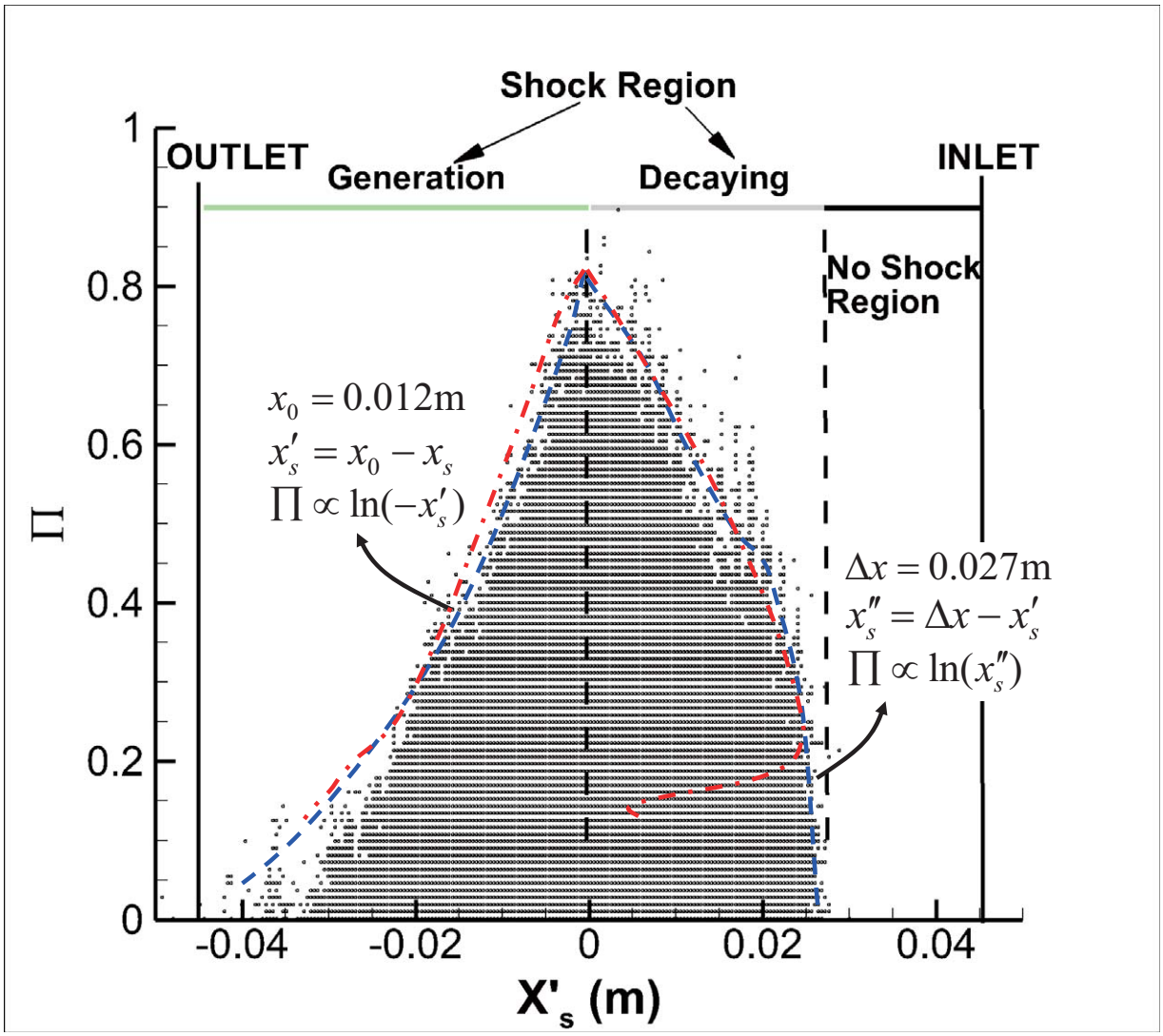

Accepted to Phys. Fluids 10.1063/5.0147216

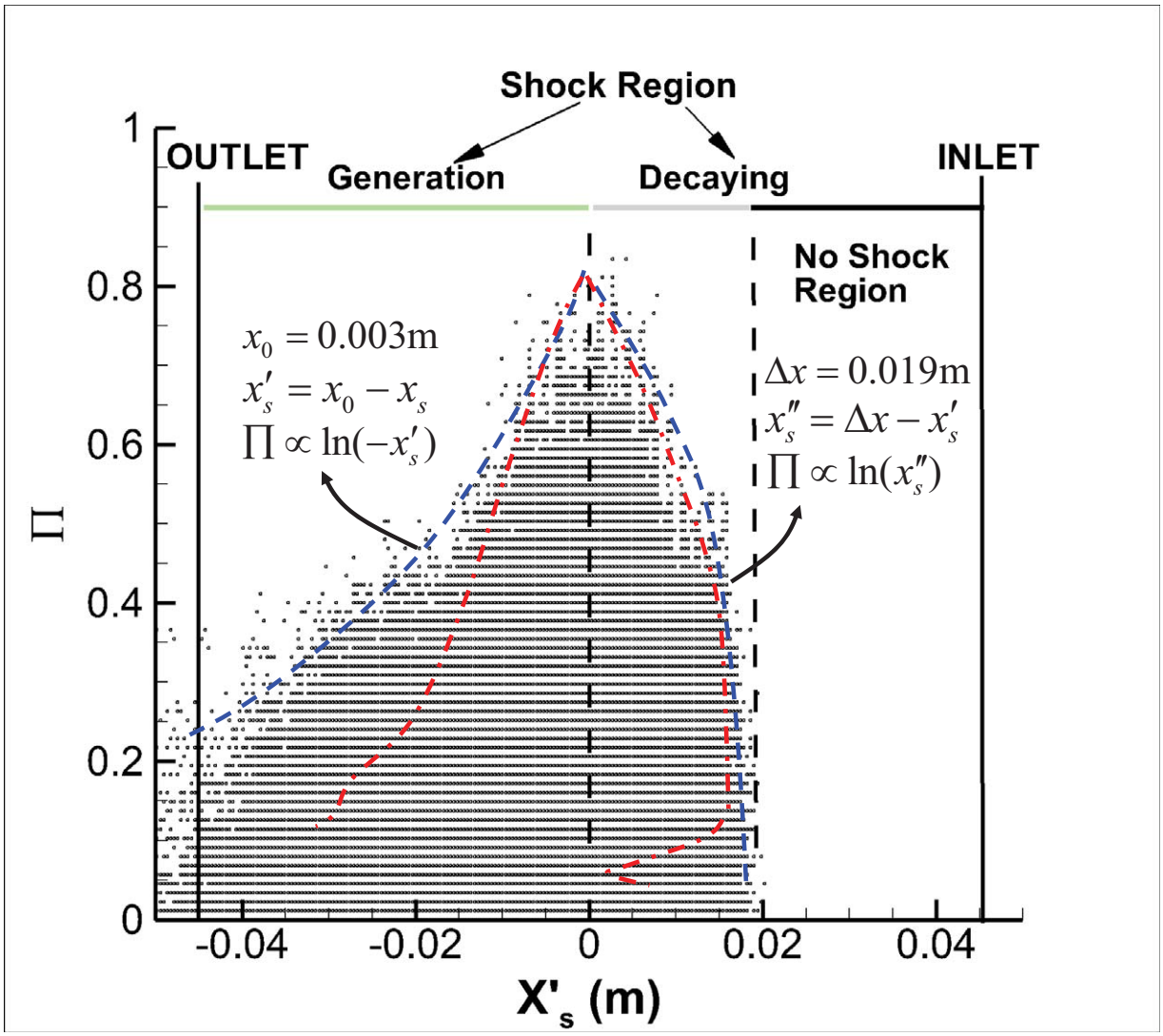

Accepted to Phys. Fluids 10.1063/5.0147216

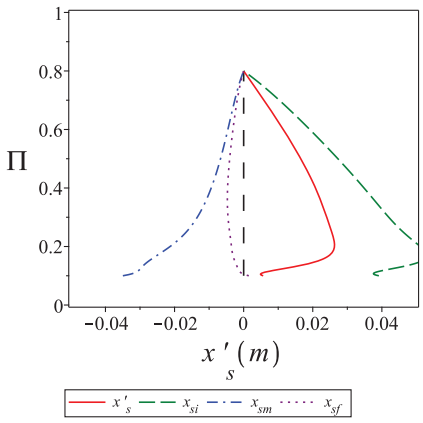

(a) Normal flow fluctuations.

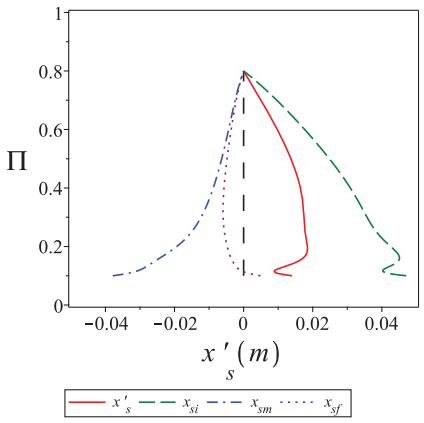

(b) Extra flow fluctuations.

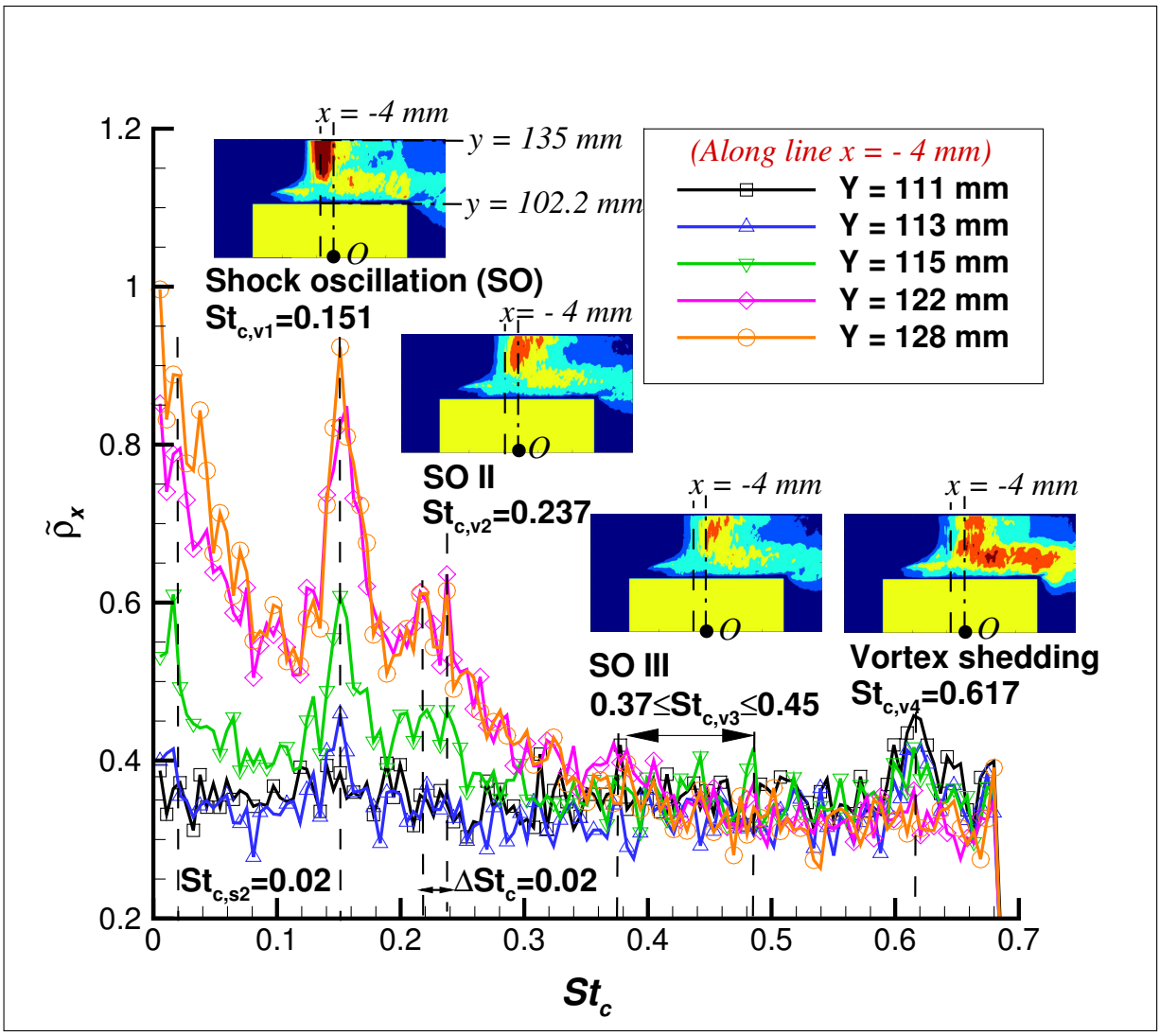

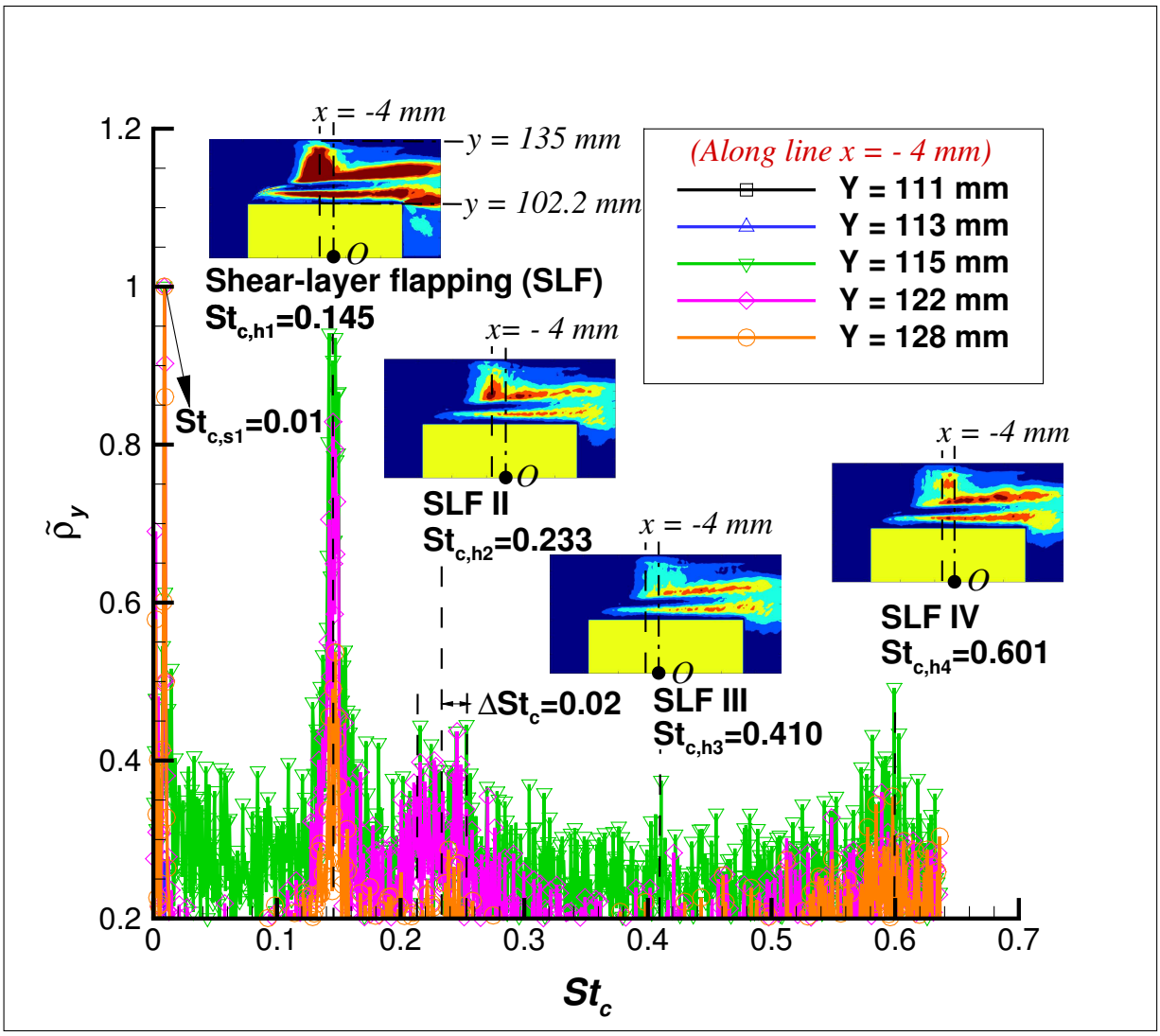

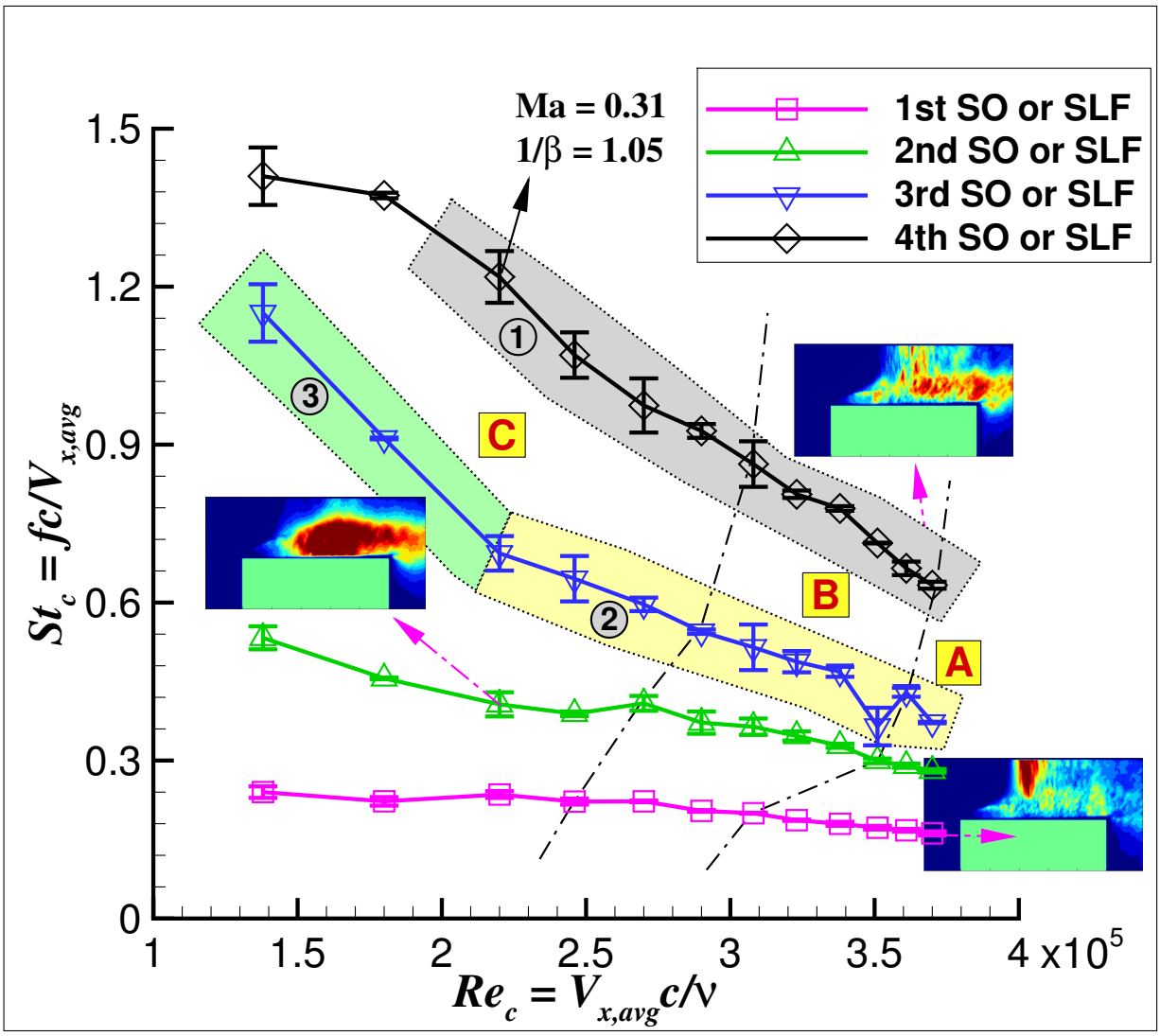

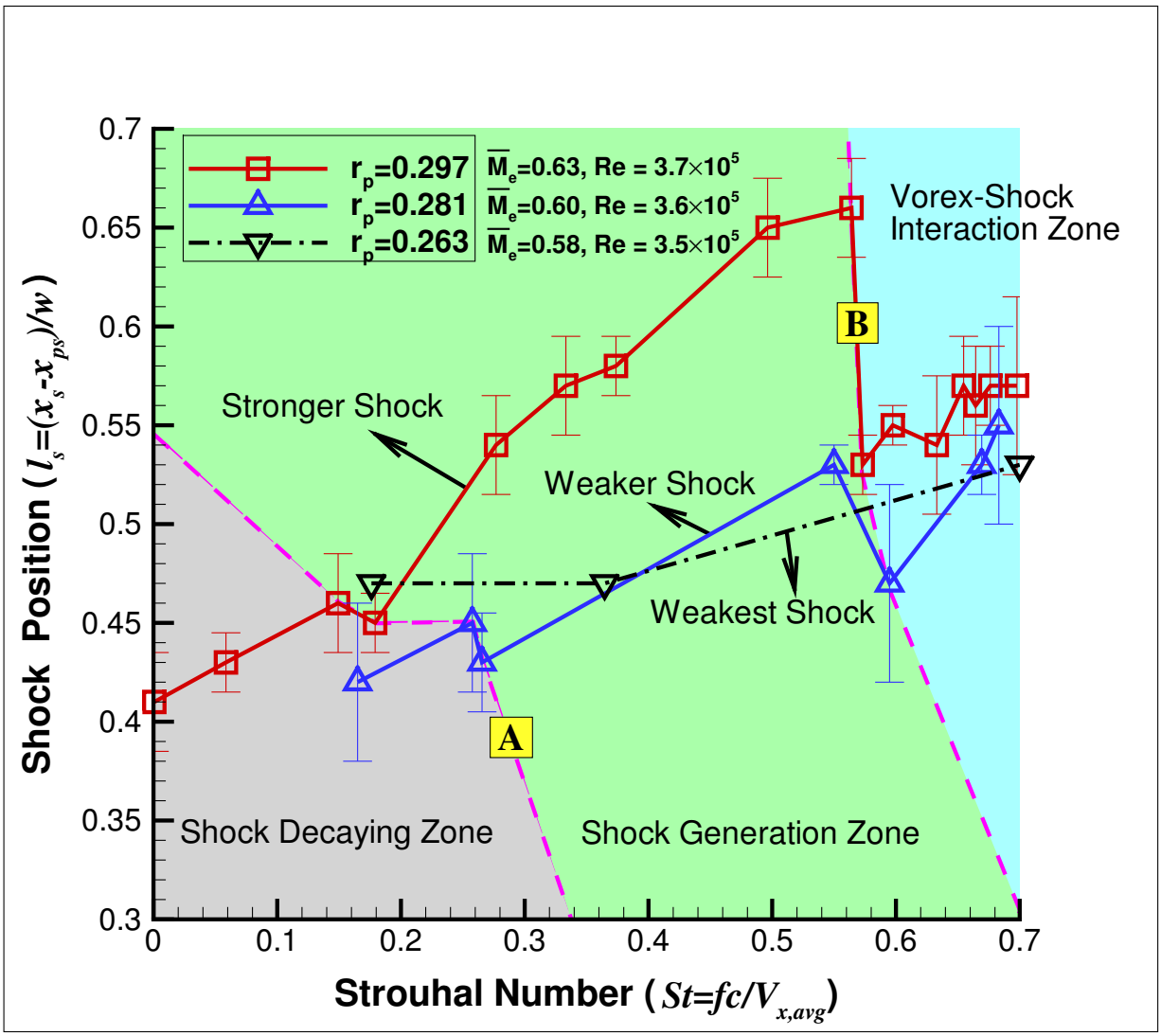

Accepted to Phys. Fluids 10.1063/5.0147216

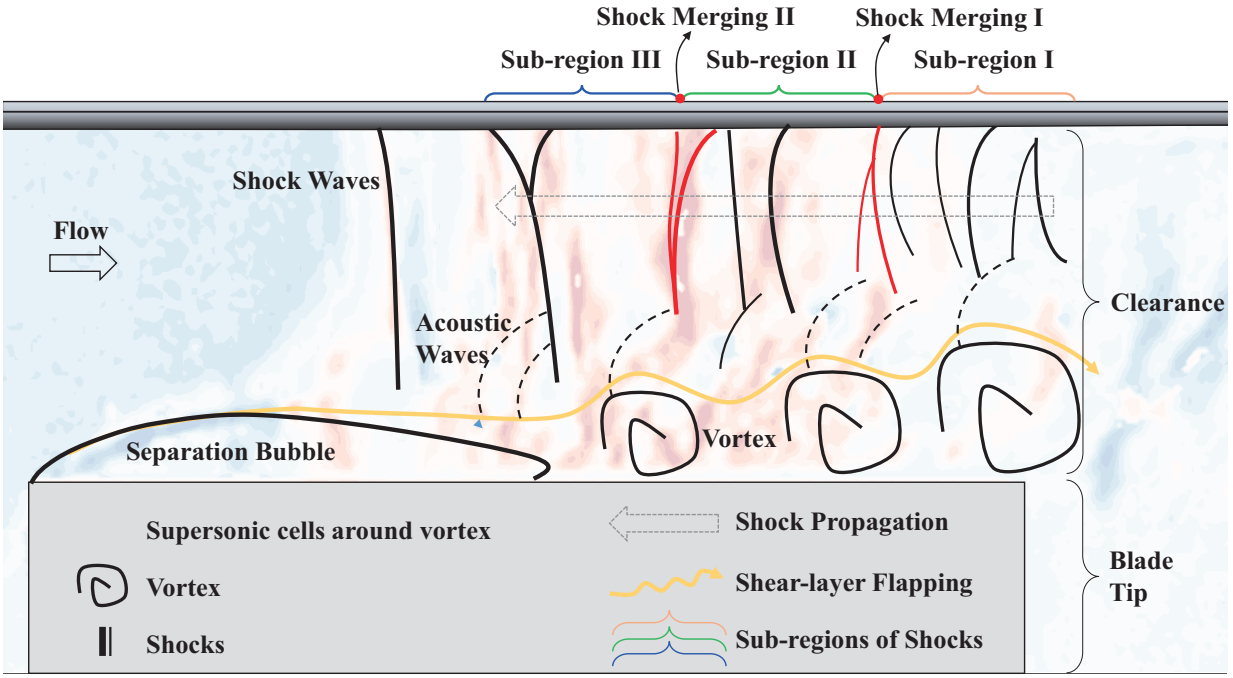

Accepted to Phys. Fluids 10.1063/5.0147216

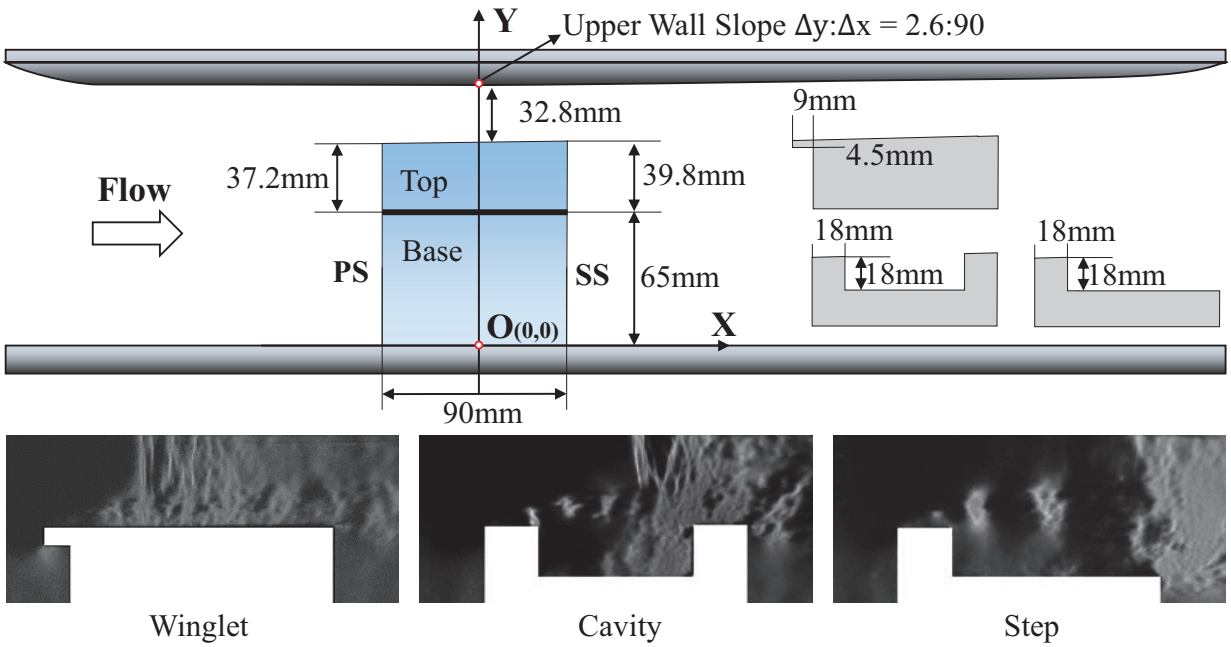

Accepted to Phys. Fluids 10.1063/5.0147216

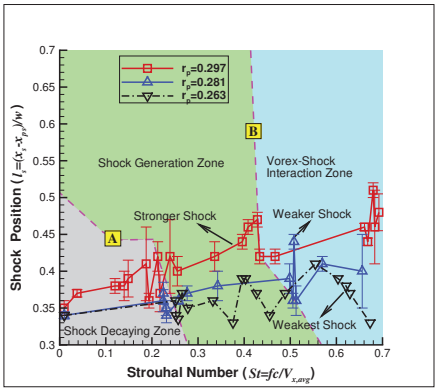

(a) Winglet.

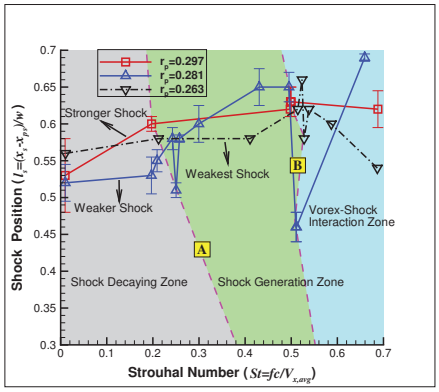

(b) Cavity.

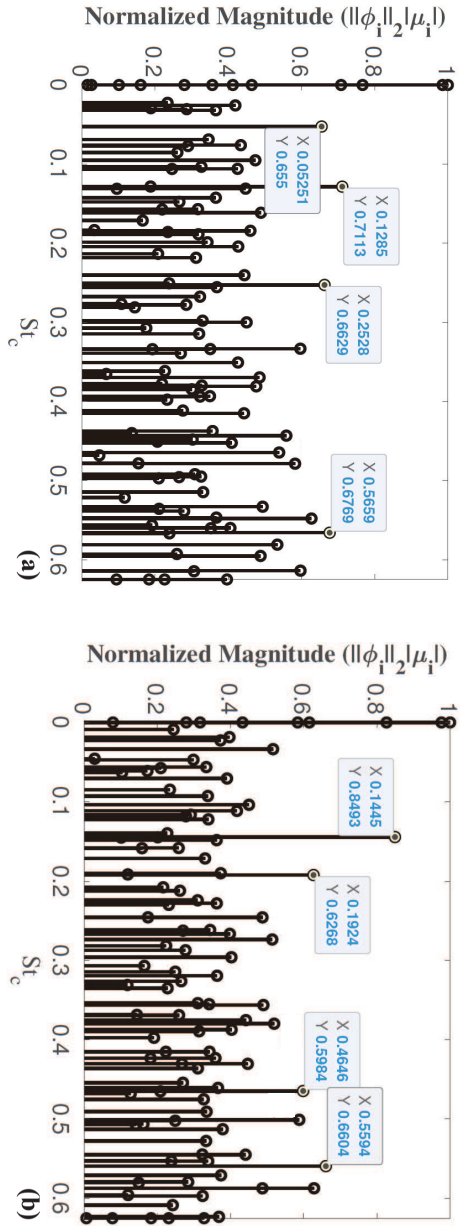

Accepted to Phys. Fluids 10.1063/5.0147216

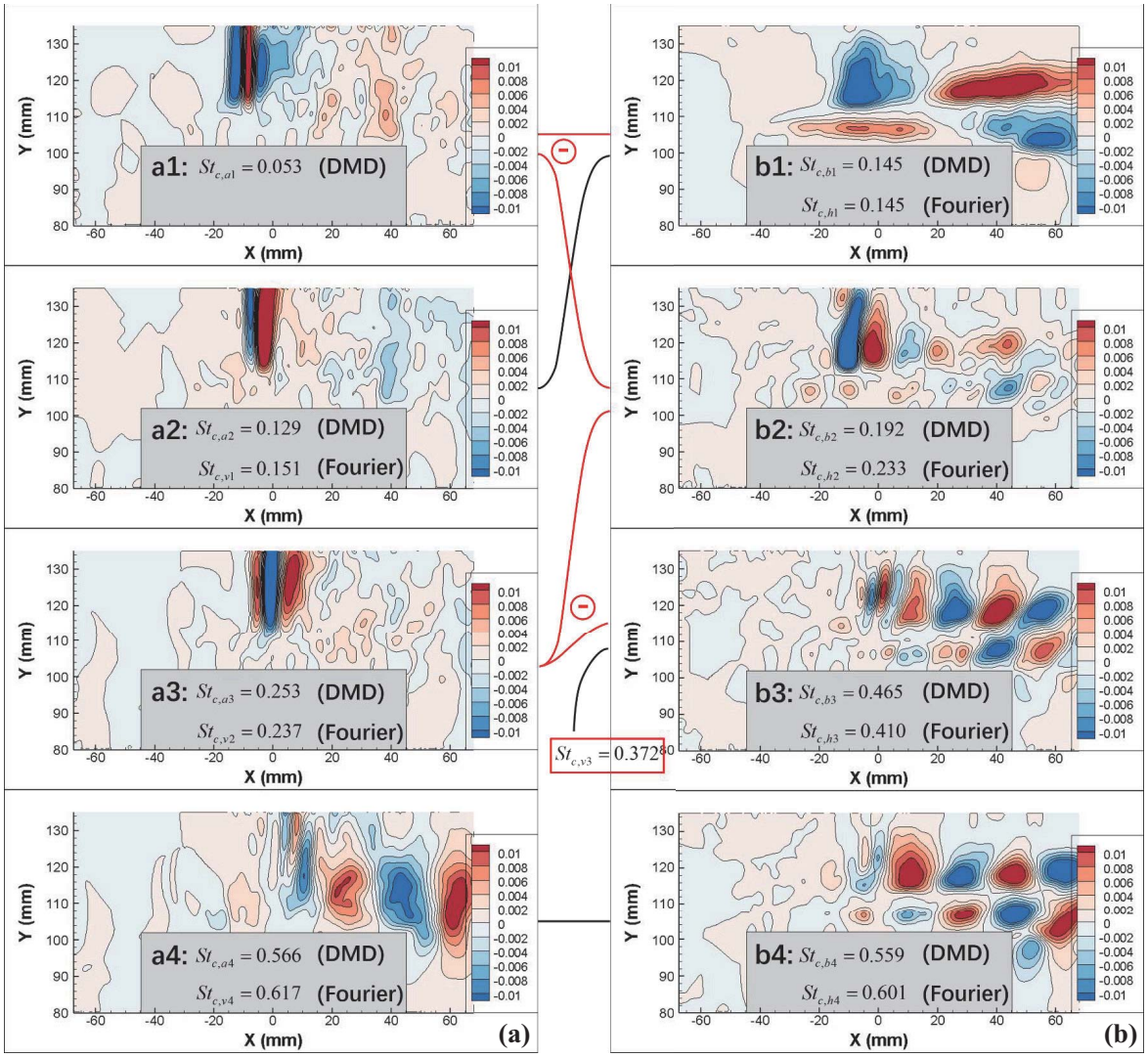

Accepted to Phys. Fluids 10.1063/5.0147216